

# Unveiling a Family of Dimerized Quantum Magnets in Ternary Metal Borides<sup>§</sup>

Zhen Zhang<sup>†,1</sup> Andrew P. Porter<sup>†,2,3</sup> Yang Sun<sup>\*,4</sup> Kirill D. Belashchenko<sup>\*,5</sup> Gayatri Viswanathan,<sup>2,3</sup> Arka Sarkar,<sup>2,3</sup> Kirill Kovnir<sup>\*,2,3</sup> Kai-Ming Ho,<sup>1</sup> and Vladimir Antropov<sup>\*,1,3</sup>

<sup>1</sup>*Department of Physics and Astronomy, Iowa State University, Ames, IA 50011, USA*

<sup>2</sup>*Department of Chemistry, Iowa State University, Ames, IA 50011, USA*

<sup>3</sup>*Ames National Laboratory, U.S. Department of Energy, Ames, IA 50011, USA*

<sup>4</sup>*Department of Physics, Xiamen University, Xiamen 361005, China*

<sup>5</sup>*Department of Physics and Astronomy and Nebraska Center for Materials and Nanoscience, University of Nebraska-Lincoln, Lincoln, NE 68588, USA*

(Dated: June 6, 2024)

Dimerized quantum magnets are exotic crystalline materials where Bose-Einstein condensation of magnetic excitations can happen. However, known dimerized quantum magnets are limited to only a few oxides and halides. Here, we unveil 9 dimerized quantum magnets and 11 conventional antiferromagnets in ternary metal borides  $MTB_4$  ( $M = \text{Sc, Y, La, Ce, Lu, Mg, Ca, Al}$ ;  $T = \text{V, Cr, Mn, Fe, Co, Ni}$ ). In this type of structure,  $3d$  transition-metal atoms  $T$  are arranged in dimers. Quantum magnetism in these compounds is dominated by strong antiferromagnetic interactions between Cr (both Cr and Mn for  $M = \text{Mg and Ca}$ ) atoms within the structural dimers, with much weaker interactions between the dimers. These systems are proposed to be close to a quantum critical point between a disordered singlet spin-dimer phase, with a spin gap, and the ordered conventional Néel antiferromagnetic phase. This new family of dimerized quantum magnets greatly enriches the materials inventory that allows investigations of the spin-gap phase. All the quantum-, conventionally-, and non-magnetic systems identified, together with experimental synthesis methods of a phase suitable for characterization, provide a platform with abundant possibilities to tune the magnetic exchange coupling by doping and study this unconventional type of quantum phase transition. This work opens up new avenues for studying the quantum magnetism of spin dimers in borides and establishes a theoretical workflow for future searches for dimerized quantum magnets in other families or types of materials.

## INTRODUCTION

Quantum magnets have attracted great interest due to their many exotic phenomena<sup>1,2</sup>. In quantum magnets, tuning the quantum phase transition across the quantum critical point (QCP) can lead to different novel states of matter. One of the simplest kinds of quantum magnets are those consisting of strongly coupled spin dimers. Antiferromagnetic (AFM) intradimer coupling results in a disordered quantum paramagnetic singlet ground state. Its first excited state is a triplet state. Interdimer interactions make the triplet bands dispersive<sup>3,4</sup>. External parameters such as magnetic field<sup>4–13</sup>, pressure<sup>14–18</sup>, and doping<sup>19,20</sup> have been shown to close the spin gap and generate magnetic order. Various descriptions for the ground state of the triplets, such as Bose-Einstein condensate<sup>4,5,7–9,21</sup>, a triplet crystal<sup>6</sup>, or a supersolid<sup>10</sup>, have been proposed. Bose-Einstein

condensation (BEC) of the bosonic triplons is a particularly interesting phenomenon<sup>2</sup> since BEC is well-known for its credit to the superconductivity of Cooper pairs and the superfluidity of <sup>4</sup>He. In dimerized quantum magnets, at the QCP, the singlet ground state intersects the bottom of the lowest triplet's band dispersion, where BEC happens<sup>4</sup>. Exploring novel quantum magnets and states of matter in the vicinity of the QCP is of great significance.

So far, dimerized quantum magnets have been discovered, and the associated BEC have been studied<sup>2</sup> mostly in oxides and halides such as  $\text{BaCuSi}_2\text{O}_6$ <sup>4,8,9,22</sup>,  $\text{Ba}_3\text{Mn}_2\text{O}_8$ <sup>11–13,23</sup>, and  $\text{TlCuCl}_3$ <sup>5,7,14–19</sup>. Quantum spin dimers have yet been scarcely discovered and reported in boron compounds. Boron compounds are versatile due to their unusual electronic<sup>24</sup>, magnetic<sup>24,25</sup>, and structural<sup>26</sup> properties. For example, boron nitride (BN) is a chemical analog to carbon; both are expected to adopt similar one-, two-, and three-dimensional structures<sup>27</sup>. Borides are often reported to be suitable for high-temperature ferromagnets<sup>28–31</sup>, catalysis<sup>32–34</sup>, thermoelectricity<sup>35</sup>, and superhard materials<sup>36–39</sup>. Superconductivity has been discovered in magnesium diboride ( $\text{MgB}_2$ )<sup>40–43</sup>.  $\text{Nd}_2\text{Fe}_{14}\text{B}$  is one of today's best-performing permanent magnets<sup>44</sup>. The formation of binary, ternary, and multinary borides among boron and metal elements provides a rich materials family to explore.

<sup>§</sup> This document is the unedited Author's version of a Submitted Work that was subsequently accepted for publication in Journal of the American Chemical Society, copyright © 2024 American Chemical Society after peer review. To access the final edited and published work see <https://pubs.acs.org/doi/10.1021/jacs.4c05478>.

<sup>†</sup> Equal contribution.

<sup>\*</sup> Email: yangsun@xmu.edu.cn (Y.S.); belashchenko@unl.edu (K.D.B.); kovnir@iastate.edu (K.K.); antropov@iastate.edu (V.A.).

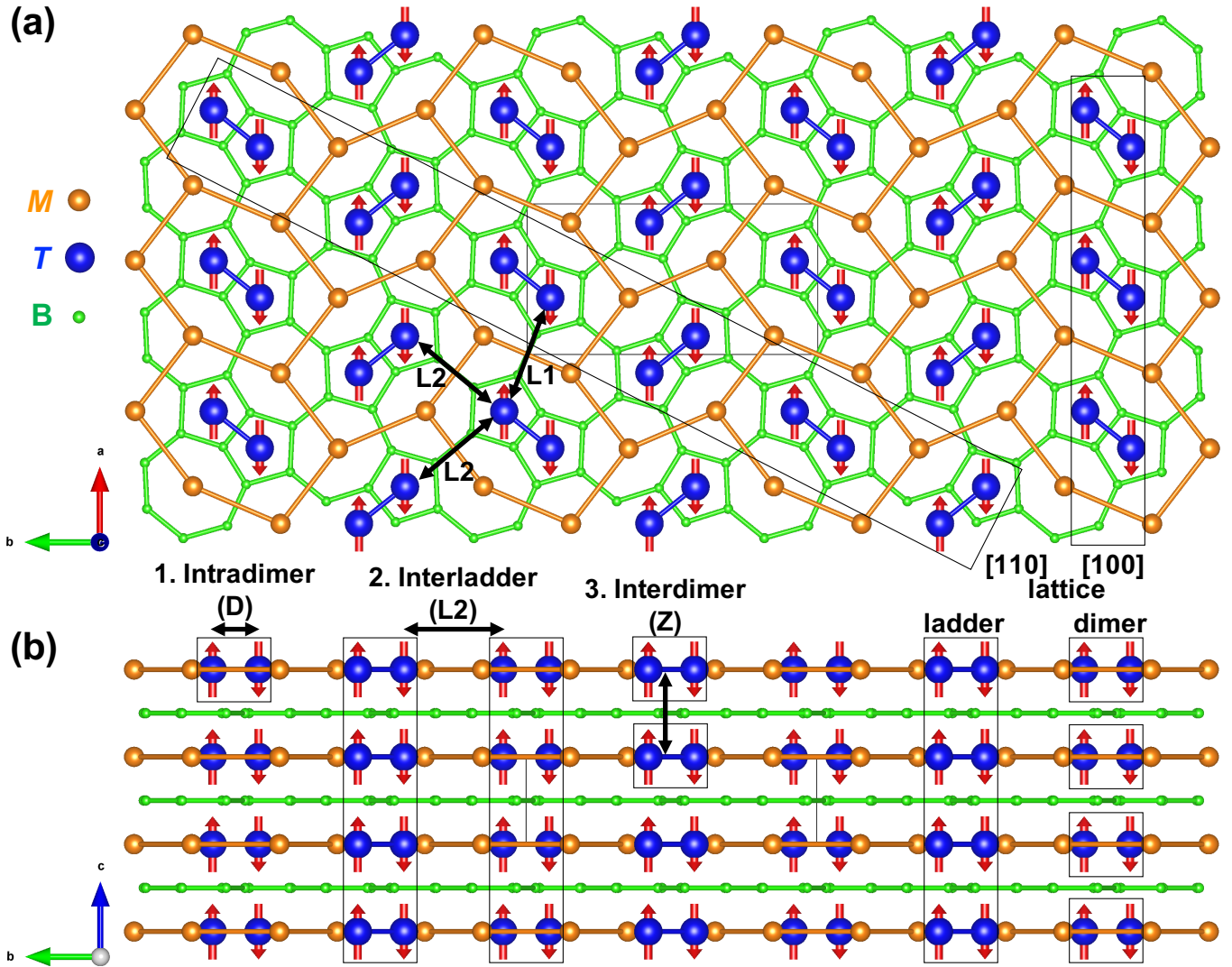


FIG. 1. YCrB<sub>4</sub>-type crystal structure. (a) [001] and (b) [100] projections. Orange, blue, and green spheres show *M*, *T*, and *B* atoms, respectively. Red arrows show magnetic moments. AFF magnetic ordering is displayed in the figure as an example. The three-letter notation for the magnetic configuration indicates the relative alignment of the local moments inside a dimer (D), between the nearby dimers in the same plane (L2), and between the neighboring layers (Z).

Driven by the idea to seek quantum spin dimers in borides, we uncover the family of compounds with YCrB<sub>4</sub>-type structure. YCrB<sub>4</sub> was reported to offer promising physical properties such as thermoelectricity<sup>45,46</sup> and high mechanical strength<sup>47–49</sup>. This class of materials, i.e., metal (*M*) - transition metal (*T*) - tetraborides (B<sub>4</sub>), was reported by early experimental studies<sup>50,51</sup>. ScTB<sub>4</sub> (*T* = Fe, Co, Ni), YTB<sub>4</sub> (*T* = V, Cr, Mn, Fe, Co), CeTB<sub>4</sub> (*T* = Cr, Mn, Fe, Co), and LuTB<sub>4</sub> (*T* = Cr, Fe, Co, Ni) were briefly mentioned<sup>50–54</sup>. However, methods to produce single-phase samples suitable for characterization are known only for a subset of the reported compounds. On the other hand, theoretical investigations of the fundamental electronic and magnetic properties of these compounds are scarce, even for the prototypical YCrB<sub>4</sub><sup>46,47,55</sup>.

Previous first-principles calculations for YCrB<sub>4</sub> show non-magnetic<sup>46,47</sup> (NM) and semiconducting<sup>46,47,55</sup> behavior. A remarkable structural feature of this class of materials is a transition-metal dimer formation. How such a transition-metal dimer formation quantum mechanically impacts the materials' electronic and magnetic properties is unknown and to be explored.

In this study, we utilize first-principles calculations to study the electronic and magnetic properties of *MTB*<sub>4</sub>, where *M* is IIIB metals (Sc, Y, La, Ce, Lu) and *T* is 3*d* transition metals (V, Cr, Mn, Fe, Co, Ni). The NM IIIB elements are considered to eliminate the magnetic effects arising from the *M* atoms on the transition-metal dimers. Sc<sup>3+</sup>, Y<sup>3+</sup>, La<sup>3+</sup>, and Lu<sup>3+</sup> all have a close-valence shell structure; thus, their formed *MTB*<sub>4</sub> compounds are expected to show similar physical properties. Our previous

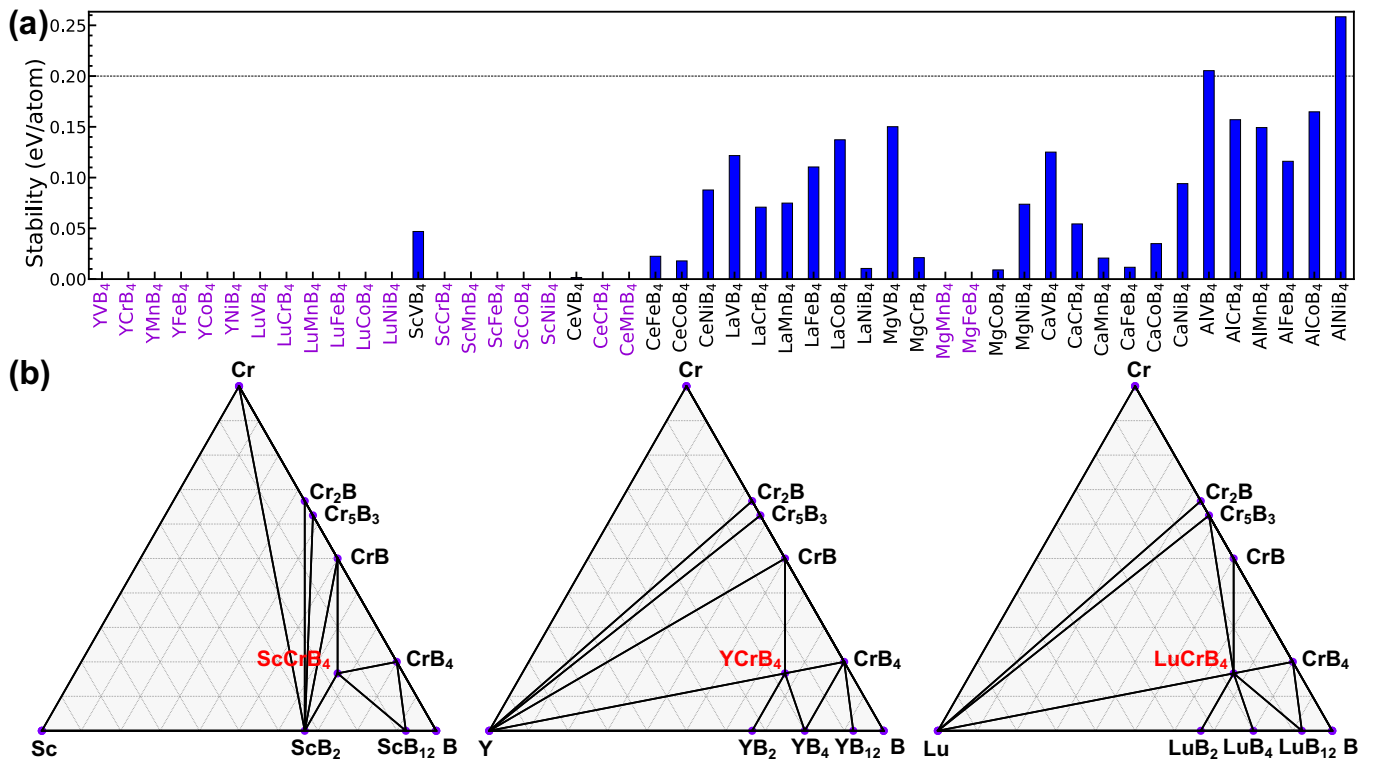


FIG. 2. Phase stability. (a) Stability of  $MTB_4$ . Purple x-labels indicate stable compounds. (b) Convex hulls for  $M$ -Cr-B ( $M = \text{Sc}, \text{Y}, \text{Lu}$ ).

study<sup>56</sup> generalized  $M$  in this class of materials to the main-group elements, Mg, Ca, and Al. However, whether they are quantum magnets remains to be studied. In this work, we investigate the quantum magnetism for this entire generalized family of materials.

From the synthesis point of view,  $YCrB_4$  is the compound that gives the name to this structure type.  $YCrB_4$  and  $YMnB_4$  have been experimentally synthesized in single-phase form, and their crystal structures were reported together with some conventional properties<sup>45,46,49–51</sup>. In turn,  $YFeB_4$  and  $YCoB_4$  have been only briefly mentioned without properly describing the experimental synthetic procedures. In this study, experimental efforts are focused on the synthesis of  $YFeB_4$  and  $YCoB_4$  and the characterization of their structure and basic properties. Synthetic and computational approaches were developed in parallel in this work to further future studies of abundant quaternary borides containing two IIIB metals or two  $3d$  metals, i.e., doping on the  $M$  site or the  $T$  site.

## RESULTS AND DISCUSSION

**$YCrB_4$ -Type Crystal Structure.** The  $YCrB_4$ -type crystal structure is displayed in Figure 1. It crystallizes in the  $Pbam$  space group with a layered structure, consisting of alternating sheets of boron atoms and metal atoms. The sheet of boron atoms forms a tiling of pentagons and heptagons. The sheet of metal atoms con-

sists of a tiling of squashed hexagons of  $M$  atoms with a transition-metal dimer inside each hexagon. Take  $YTB_4$ , for example. The intradimer distances ( $D$ ) are  $\sim 2.3$ – $2.6$  Å for different  $T$  elements. Dimers form ladders in the direction perpendicular to the plane ( $[001]$ ). Dimer-dimer separation along the ladder ( $Z$ ) is  $\sim 1.4 D$ . Ladders make up a two-dimensional lattice in directions parallel to the plane ( $[110]$ ,  $[1\bar{1}0]$ , or  $[100]$ ). Ladder-ladder separation ( $L1, L2$ ) is  $\sim 2 D$ . (Each  $T$  atom has one  $L1$  and two  $L2$  neighbors at very similar distances.) Since the intradimer distance is the shortest among the three, intradimer interaction should be the strongest interaction among the  $T$  atoms.

**Phase Stability.** The formation energy ( $E_f$ ) is obtained from spin-polarized calculations. Then, the formation energy relative to the convex hull ( $E_d$ ) is evaluated by the formation energy differences with respect to the three reference phases forming the Gibbs triangle on the convex hull. The reference phases on the convex hulls are obtained from materials databases such as Materials Project<sup>57</sup> and OQMD<sup>58</sup>. All phases are fully relaxed, and the total energies are calculated using the same density-functional theory (DFT) settings. If an  $MTB_4$  phase has  $E_d < 0$ , then it is stable. In this case, the convex hull is reconstructed to include the  $MTB_4$ 's  $E_f$ , and the  $MTB_4$ 's stability is denoted as zero. If an  $MTB_4$  phase has  $E_d > 0$ , then it is not stable. In this case, the  $MTB_4$ 's stability indicates the distance above the convex hull. The

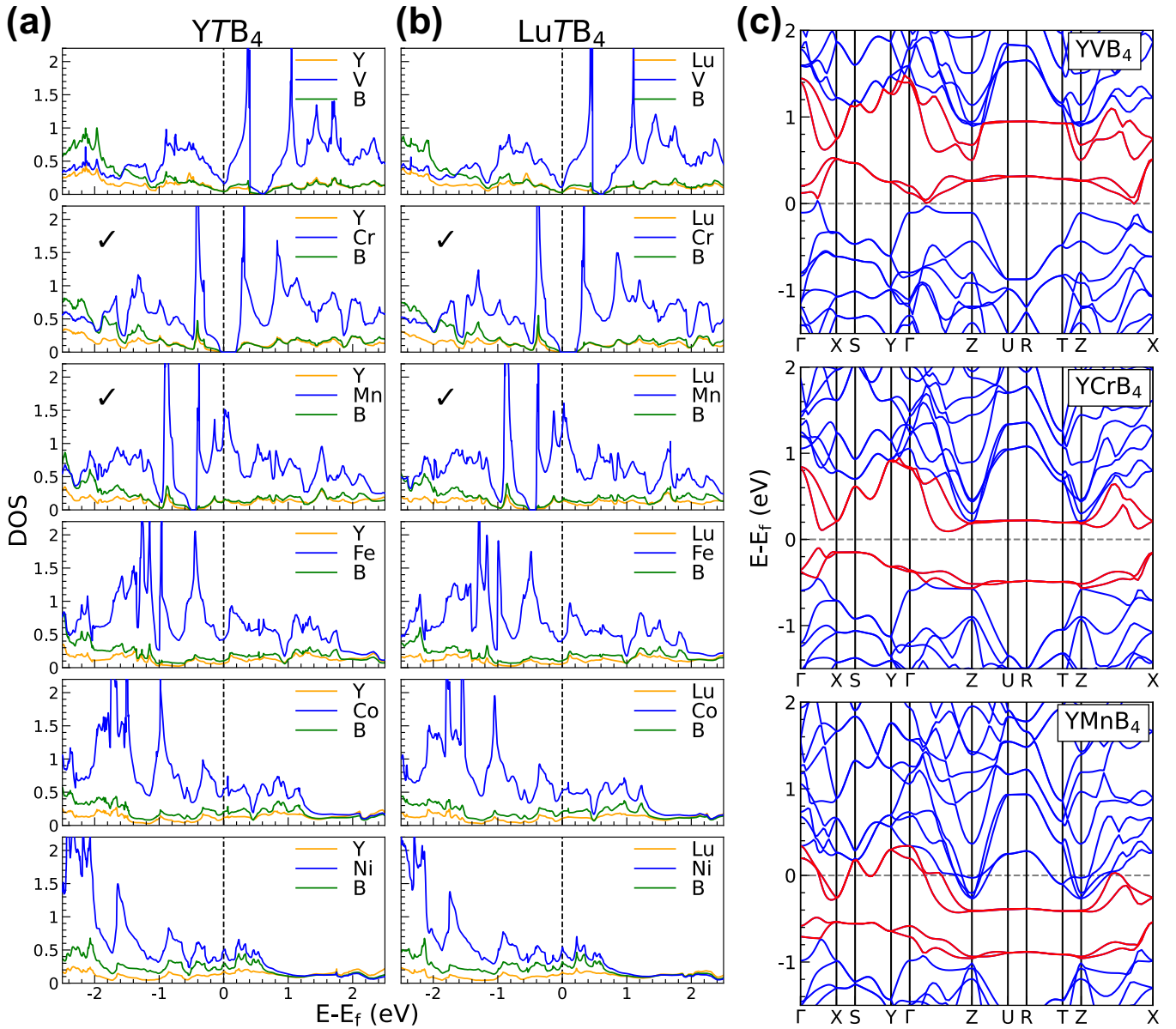


FIG. 3. Non-magnetic (NM) electronic structures. Density of states ( $\text{eV}^{-1} \text{f.u.}^{-1} \text{spin}^{-1}$ ) for (a)  $\text{YTB}_4$  and (b)  $\text{LuTB}_4$  ( $T = \text{V, Cr, Mn, Fe, Co, and Ni}$ ). Orange, blue, and green curves represent partial DOS of  $M$ ,  $T$ , and  $B$  atoms, respectively. Check marks indicate systems with stable magnetic solutions. (c) Band structure for  $\text{YTB}_4$  ( $T = \text{V, Cr, and Mn}$ ). High-symmetry points in the Brillouin zone are denoted as follows:  $\Gamma(0, 0, 0)$ ,  $X(1/2, 0, 0)$ ,  $S(1/2, 1/2, 0)$ ,  $Y(0, 1/2, 0)$ ,  $Z(0, 0, 1/2)$ ,  $U(1/2, 0, 1/2)$ ,  $R(1/2, 1/2, 1/2)$ ,  $T(0, 1/2, 1/2)$ . Red color highlights nearly flat bands in the Brillouin zone corresponding to two narrow peaks in the NM DOS.

calculated stabilities of all  $\text{MTB}_4$  are shown in Figure 2a. Stability = 0 indicates a stable phase. We use  $0.2 \text{ eV/atom}^{59}$  as the criterion for choosing metastable compounds that are possibly stabilized by thermodynamics. Then, we obtain 21 stable and 25 metastable compounds in  $\text{MTB}_4$ . The calculated convex hulls for  $M\text{-Cr-B}$  ( $M = \text{Sc, Y, and Lu}$ ) systems are exhibited in Figure 2b.

**Electronic Properties of the Non-Magnetic (NM) States.** The NM density of states (DOS) for the representative Y and Lu compounds are plotted in Figure 3, and the DOS at the Fermi level  $N(E_f)$  are listed in

Table 1. Due to limited space, our discussion will mainly focus on Y compounds. Other compounds have been analyzed similarly.  $N(E_f)$  of these compounds are mainly contributed by the  $T$  atom. V has a low DOS at the Fermi level, making V compounds weakly metallic. Fe, Co, and Ni have  $N(E_f) \sim 0.5 \text{ eV}^{-1} \text{f.u.}^{-1} \text{spin}^{-1}$ . Hence, these compounds are “good” metals. For Fe, the Fermi level is at the minimum of DOS, but there is a peak right above it. Applying some strain or doping may move the Fermi level toward this peak. For Ni, the Fermi level is located at a minor peak. In contrast, for Mn, the Fermi



TABLE I. Density of states (DOS) of transition metals  $N_T(E_f)$  ( $\text{eV}^{-1} \text{f.u.}^{-1} \text{spin}^{-1}$ ) and total DOS  $N_{\text{tot}}(E_f)$  ( $\text{eV}^{-1} \text{f.u.}^{-1} \text{spin}^{-1}$ ) at the Fermi level for  $YTB_4$  and  $LuTB_4$ .

Compound	$N_T(E_f)$	$N_{\text{tot}}(E_f)$	Compound	$N_T(E_f)$	$N_{\text{tot}}(E_f)$
YVB <sub>4</sub>	0.165	0.331	LuVB <sub>4</sub>	0.117	0.230
YCrB <sub>4</sub>	0.0	0.0	LuCrB <sub>4</sub>	0.0	0.0
YMnB <sub>4</sub>	1.209	1.696	LuMnB <sub>4</sub>	1.194	1.656
YFeB <sub>4</sub>	0.425	0.680	LuFeB <sub>4</sub>	0.417	0.667
YCoB <sub>4</sub>	0.537	1.016	LuCoB <sub>4</sub>	0.516	0.972
YNiB <sub>4</sub>	0.488	1.142	LuNiB <sub>4</sub>	0.530	1.210

level is at a sharp peak of DOS, suggesting a strong electronic instability.

The NM DOS for YCrB<sub>4</sub> shows a semiconducting character with a narrow band gap of 0.20 eV, which agrees with the experimental estimate of 0.17 eV<sup>45</sup>. The semiconducting character of NM YCrB<sub>4</sub> agrees with previous first-principles calculations<sup>46,47,55</sup>, which reported a gap of 0.05 eV<sup>55</sup>,  $0.14 \pm 0.04$  eV<sup>46</sup>, and 0.17 eV<sup>47</sup>.

A remarkable feature in the NM DOS of these compounds is the presence of two narrow peaks, which are both empty in V, straddle the Fermi level in Cr, and both filled in Mn compounds. These narrow peaks displayed in the electronic spectrum are known as Van Hove singularities (VHS). Generally, VHS near the Fermi level can lead to instabilities, such as charge density waves, and induce phase transitions under changing temperature, pressure, or chemical doping. They can also be associated with interesting optical properties and with large DOS near the Fermi level, the latter of which tends to enhance superconductivity. Understanding the presence and influence of VHS is valuable in the design and engineering of new materials.

These VHS result from two pairs of bands, highlighted in red in Figure 3, that are nearly flat on the  $k_z = 1/2$  plane (Z-U-R-T-Z path in Figure 3). The flat bands are formed by  $d_{z^2}$  orbitals of the transition-metal atoms<sup>46</sup>, and the two pairs of bands correspond to bonding and antibonding states of the dimers. (Two bands in each pair correspond to two dimers per unit cell.) For a generic wavevector, the dimer states can hybridize with B atoms, leading to significant dispersion visible along the  $\Gamma$ -X-S-Y- $\Gamma$ -Z path. However, this hybridization is suppressed at  $k_z = 1/2$  due to the destructive interference between the hopping amplitudes for the two transition-metal sheets to the  $s$ ,  $p_x$ , and  $p_y$  orbitals of the B atoms. This cancellation effectively localizes the dimer states with  $k_z = 1/2$ , leading to flat bands and the corresponding peaks in the DOS. The strength of the interdimer hybridization determines the width of the peaks and is, therefore, much smaller (at about 0.2 eV for Cr compounds) than in Cr metal, where it is in the range of 1-2 eV.

The DOS for the different transition metals exhibits an approximately “rigid band” behavior. By tuning electron concentration and changing the transition metal from V

to Mn, the DOS plots show similar patterns with the Fermi level located below, in between, and above the two major VHS, respectively. Such a “rigid band” behavior is common for similar systems<sup>56</sup>.

**Magnetic States.** VHS near the Fermi level may be associated with various electronic instabilities. Based on the analysis of the real-space paramagnetic Pauli spin susceptibility matrix (see Methods), we consider magnetic orderings with ferromagnetic (FM) or antiferromagnetic (AFM) alignment of the local moments within a dimer, between the nearby dimers in the same plane, and between the adjacent layers (see Figure 1). We will use a three-letter notation consisting of letters F (for FM) and A (for AFM) to denote these orderings, such as AFF, where each letter identifies the alignments in this particular order. The labeling of the first and the third letters is straightforward. A few comments are in order about the in-plane interladder ordering, which is indicated by the second letter. (1) It indicates the ordering between dimers along the L2 but not L1 direction (see Figure 1). (2) The alignment is identified by comparing spins between DL2, which is the linked path of D and L2. (3) The A ordering is similar to the stripe ordering on the hexagonal lattice. The specific ordering patterns are displayed in Figure 4.

Eight magnetic configurations are obtained through all possible combinations of these alignments and are considered in the calculations. For example, AFF means intradimer AFM, interladder FM, and interlayer FM coupling. The AFF configuration is displayed in Figure 1. However, not all of these configurations are stable; many do not have a self-consistent DFT solution with finite magnetic moments.

Figure 4a shows all the stable magnetic solutions for  $MTB_4$ , with the eight magnetic configurations illustrated in Figure 4b. The top panel of Figure 4a shows the stabilization energy relative to the NM state, and the bottom panel shows the magnetic moment on the T atoms. Compounds without any magnetic solutions are not shown. In total, we find 20 magnetic compounds, among which 10 are stable (purple x-labels in Figure 4a) and 10 are metastable (black x-labels). Strong AFM intradimer exchange and weak interdimer interactions result in quantum spin-gap systems. According to the alignment of intradimer coupling of the DFT ground state, we group these compounds into two categories: quantum spin-dimer magnets and conventional magnets (see Figure 4). Such categorization immediately justifies itself. It is clear that the DFT ground state always has the same intradimer spin alignment, indicated by the symbol color, as those of multiple low-energy states. Such a phenomenon results from the dominating intradimer coupling strength compared to the interdimer ones. Dimerized quantum magnets own AFM intradimer spin alignments (red symbols in Figure 4) as DFT ground state and low-energy states, while conventional magnets own FM intradimer spin alignments (blue symbols) as ground and low-energy states.

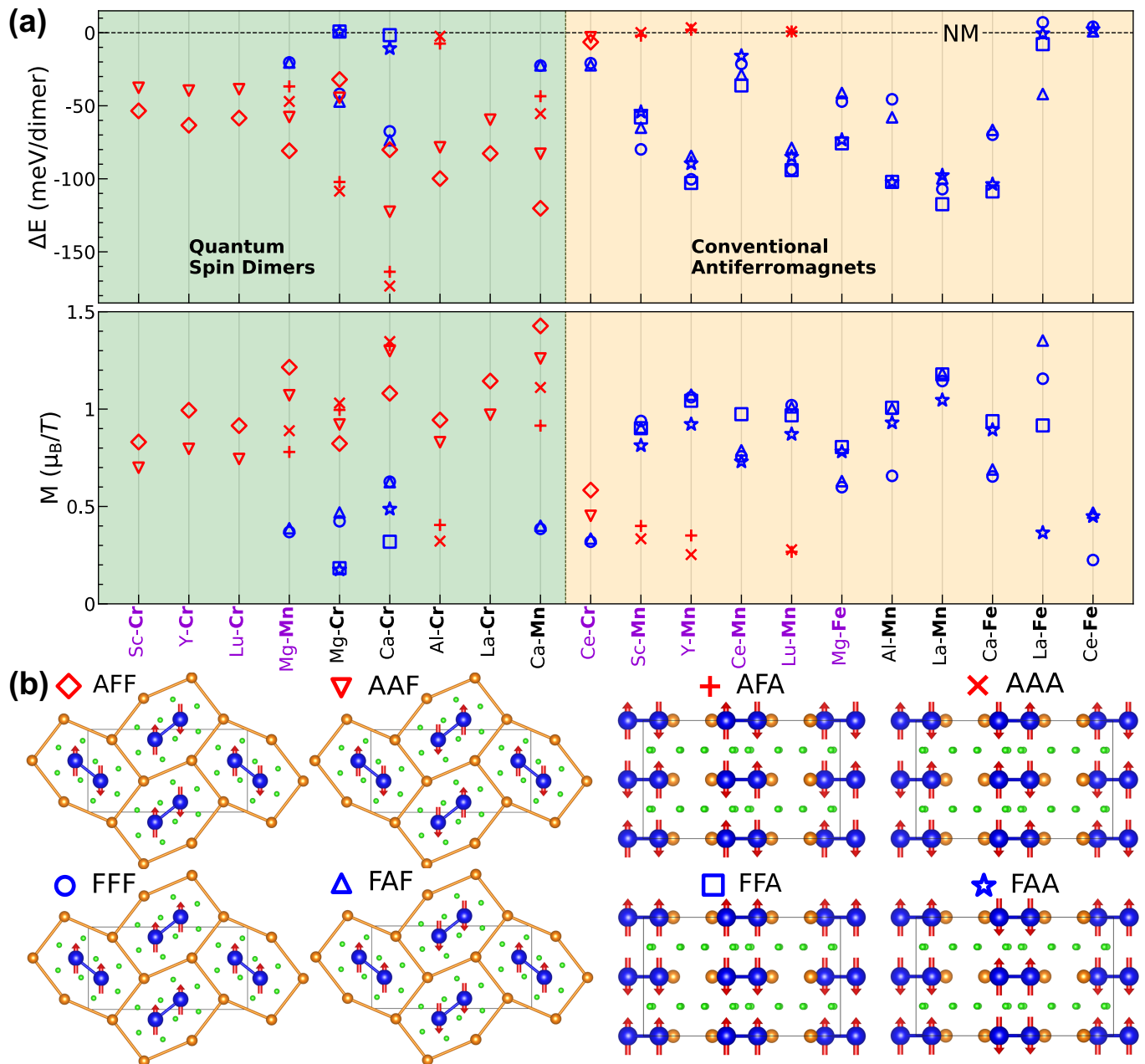


FIG. 4. The DFT magnetic solutions. (a) The relative energy difference of the magnetic solutions to the NM one (top) and the magnetic moment on the transition metal  $T$  (bottom) for  $MTB_4$ . The green and orange regions indicate quantum spin dimers and antiferromagnets, respectively. Purple and black x-labels indicate stable and metastable compounds, respectively. (b) Different magnetic configurations and the associated symbols and labels.

We identify a total of 9 quantum spin-dimer magnets and 11 conventional magnets. Note although the ground states of the conventional magnets have FM intradimer ordering, they are still overall AFM with zero net spins. The only exception is  $ScMnB_4$ , the ground state of which is overall FM (FFF). Considering the closeness of its energy to other AFM states, we do not specifically distinguish this one and denote all the conventional magnets as conventional antiferromagnets. Remarkably, compounds with the same valence shell electron count belong to the

same magnets category and exhibit a similar distribution of magnetic solutions. Cr forms a quantum AFM dimer with two ordered solutions when combined with  $Sc^{3+}$ ,  $Y^{3+}$ ,  $La^{3+}$ , and  $Lu^{3+}$ . Mn forms a conventional FM dimer with four well-defined magnetic solutions when combined with  $Sc^{3+}$ ,  $Y^{3+}$ ,  $La^{3+}$ , and  $Lu^{3+}$ . V, Fe, Co, and Ni are NM when combined with these IIIB elements. Accordingly, the main-group element  $Al^{3+}$  makes Cr quantum and Mn conventional with similar distributions of magnetic solutions. Analogously, when it comes

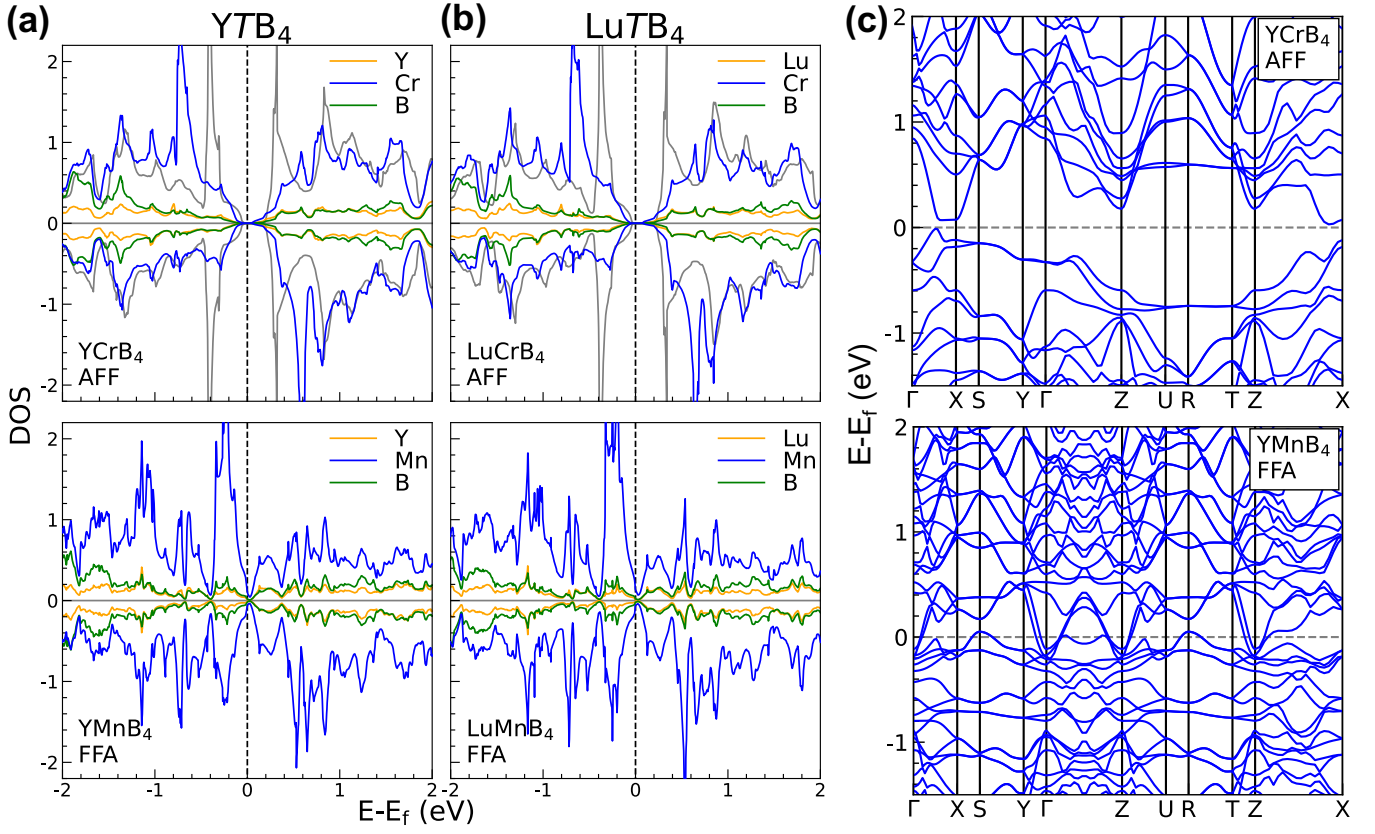


FIG. 5. Magnetic electronic structures. The partial spin-polarized density of states (in  $\text{eV}^{-1} \text{f.u.}^{-1} \text{spin}^{-1}$ ) of the DFT ground state of (a)  $\text{YTB}_4$  and (b)  $\text{LuTB}_4$ .  $T = \text{Cr}$  has AFF solution, and  $T = \text{Mn}$  has FFA solution. Positive (negative) DOS indicates majority (minority) spin. The corresponding NM partial DOS for a Cr atom is displayed as gray curves for comparison. (c) Spin-polarized electronic band structure for the magnetic ground-state  $\text{YCrB}_4$  (top) and  $\text{YMnB}_4$  (bottom).

to  $\text{Mg}^{2+}$  and  $\text{Ca}^{2+}$ , Mn and Fe play the same role as Cr and Mn, respectively, for the 3+ elements. Therefore, Mn forms quantum spin dimers when combined with  $\text{Mg}^{2+}$  and  $\text{Ca}^{2+}$ , and Fe forms FM spin dimers with  $\text{Mg}^{2+}$  and  $\text{Ca}^{2+}$ . In turn, Cr plays the same role as V but is not as silent as V. Cr forms extra quantum spin dimers when combined with  $\text{Mg}^{2+}$  and  $\text{Ca}^{2+}$ . Ce case is more complicated due to the issue of  $4f$  electron localization. GGA+U may be required, which may change the current results for Ce. We leave this to future study and only report Ce's magnetism by GGA here.

Next, we analyze the magnetic solutions for the representative Y and Lu compounds in detail. Earlier calculations predicted these systems to be NM<sup>46,47</sup>. However, we find the DFT ground states to be AFF for Cr and FFA for Mn. In their respective DFT ground states, the magnetic moments on Cr and Mn atoms are close to  $1 \mu_B$ . Besides the ground states, self-consistent magnetic solutions were found in Cr and Mn compounds with AAF ordering for Cr and FFF, FAF, FAA, AFA, and AAA orderings for Mn. Among these, the AFA and AAA solutions for Mn have small magnetic moments of about  $0.3 \mu_B$  and the total energies are very close to the NM solution. It may indicate a weak magnetic moment de-

pendence for the energy surface near the NM state, which could enhance magnetic fluctuations.

Focusing on the solutions with well-defined magnetism,  $\text{YMnB}_4$  has stable magnetic solutions in all configurations with FM intradimer alignment (FFF, FAF, FFA, FAA), which all have similar energies (84–103 meV per dimer below the NM solution) and local moments close to  $1 \mu_B$ . This reflects the small scale of the interdimer exchange coupling compared to the intradimer coupling. AFM interlayer orderings, FFA and FAA, are more stable than FM interlayer orderings, FFF and FAF, by 2.5 and 5.2 meV per dimer, respectively. FM interladder orderings, FFF and FFA, are more stable than AFM interladder orderings, FAF and FAA, by 16 and 13 meV per dimer, respectively. On the other hand,  $\text{YCrB}_4$  has only two stable magnetic solutions, AFF and AAF, which have AFM intradimer spin alignment and energies 63 and 40 meV per dimer below the NM solution, respectively. Interestingly, Cr only has AFF and AAF solutions, indicating stable spin ladders with in-plane moment disorder with a significant energy separation of 23 meV per dimer. This energy is like that for  $\text{YMnB}_4$  (16 and 13 meV per dimer) but slightly larger. These observations for the Y compounds also apply to the Lu compounds.

TABLE II. Exchange parameters  $J_{ij}$  (in mRy) in magnetic  $MTB_4$  ( $M = Y$  and Mg).

Pair	$N_j$	AFF-YCrB <sub>4</sub>		FFA-YMnB <sub>4</sub>		AAA-MgCrB <sub>4</sub>		AFF-MgMnB <sub>4</sub>		FFA-MgFeB <sub>4</sub>	
		$R_{ij}$	$J_{ij}$	$R_{ij}$	$J_{ij}$	$R_{ij}$	$J_{ij}$	$R_{ij}$	$J_{ij}$	$R_{ij}$	$J_{ij}$
D	1	2.36	<b>-2.2</b>	2.44	2.00	2.35	<b>-1.40</b>	2.40	<b>-1.36</b>	2.42	0.94
Z	2	3.44	0.26	3.42	<b>-0.09</b>	3.25	<b>-0.02</b>	3.19	0.15	3.18	<b>-0.15</b>
DZ	2	4.17	<b>-0.40</b>	4.20	<b>0.08</b>	4.01	0.52	3.99	<b>-0.17</b>	4.00	<b>-0.14</b>
L1	1	4.83	<b>-0.02</b>	4.79	0	4.73	<b>-0.03</b>	4.70	<b>0.004</b>	4.67	0.02
L2	2	4.89	<b>-0.03</b>	4.81	-0.01	4.79	0.03	4.73	<b>-0.03</b>	4.69	-0.02
DL1	2	5.93	0	5.90	0.09	5.85	-0.06	5.83	0.02	5.79	0.09
DL2	2	5.93	-0.01	5.89	0.08	5.80	<b>-0.06</b>	5.76	-0.03	5.73	0.04
ZL1	2	5.93	<b>-0.15</b>	5.88	<b>-0.03</b>	5.74	-0.08	5.68	<b>-0.11</b>	5.65	<b>0</b>
ZL2	4	5.98	<b>-0.11</b>	5.90	<b>-0.03</b>	5.79	<b>-0.06</b>	5.71	<b>-0.10</b>	5.66	<b>-0.01</b>
$J_0$			4.54		2.59		2.94		2.49		1.98
$M$			1.01		0.91		1.00		0.93		0.68
$J_D/J_0$			-0.48		0.77		-0.48		-0.55		0.47
$ J'_0/J_D $			1.06		0.29		1.10		0.83		1.11

The three typical  $T$ - $T$  distances for the NM and DFT ground-state magnetic solutions are displayed in Figure S1 of the Supporting Information. For the NM states, D, L2, and Z show nonmonotonic trends with varying  $3d$  transition metals. For the magnetic states of the Cr and Mn systems, Z is insensitive to magnetism, whereas D is increased, and L2 is slightly decreased by magnetism. D of both AFM Cr dimers and FM Mn dimers are longer than their respective NM ones by  $\sim 0.04$  Å. This suggests that the intradimer exchange coupling in both Cr and Mn compounds is strengthened when the intradimer bond length increases, which is somewhat unusual. Note that the  $T$ - $T$  distances for different stable magnetic solutions agree with the DFT ground-state ones, and those for the two marginally stable AFA and AAA solutions for Mn are similar to those for the NM solution. Therefore, only DFT ground states of the magnetic solutions are shown.

We now examine the electronic properties of the DFT ground states. Figure 5 displays the spin-polarized DOS for the ground-state AFF Cr and FFA Mn compounds. The results for the Y and Lu compounds are very similar. AFF-ordered YCrB<sub>4</sub> is a magnetic semiconductor with a small band gap of 0.05 eV. Compared to the NM partial DOS of a Cr atom, which is shown in gray in Figure 5, the peaks in the magnetic DOS are shifted by about 0.3 eV. FFA-YMnB<sub>4</sub> is a “bad” magnetic metal with a low total DOS of 0.13 eV<sup>-1</sup> f.u.<sup>-1</sup> spin<sup>-1</sup> at the Fermi level. While Mn atoms are aligned ferromagnetically in each layer, different layers align antiferromagnetically along the z-direction. The spin-polarized band structures for the ground-state AFF-YCrB<sub>4</sub> and FFA-YMnB<sub>4</sub> are displayed alongside the DOS in Figure 5.

The DFT ground states are either semiconducting or weakly metallic for  $MTB_4$  ( $M = Y$  and Lu). The semiconducting Cr compounds in the NM state<sup>46,47,55</sup> remain semiconducting in the magnetic state. In contrast, a change from a good metal to a bad metal is seen in

Mn compounds when they switch from NM to magnetic. Considering that conventional DFT functionals such as LDA and GGA tend to underestimate the band gap, the band gaps in Cr compounds are expected to be more significant. Mn compounds can also be magnetic semiconductors.

Further, we calculate the exchange coupling parameters in the DFT ground states of  $MTB_4$  using the linear response technique<sup>60</sup> implemented within the tight-binding linear muffin-tin orbital (TB-LMTO) method in the Questaal code<sup>61</sup>. For YCrB<sub>4</sub>, we note that the magnetic moment on the Cr atoms is sensitive to computational details and is too small at 0.49  $\mu_B$  in LMTO compared to the full-potential VASP calculation (0.99  $\mu_B$ ). We correct this discrepancy by scaling the exchange-correlation field by a factor of 1.13, which increases the magnetic moment to 1.01  $\mu_B$ . Similarly, for MgCrB<sub>4</sub>, the exchange-correlation field is scaled by 1.19 to obtain the local moment of 1.00  $\mu_B$ . For YMnB<sub>4</sub>, MgMnB<sub>4</sub>, and MgFeB<sub>4</sub>, the local magnetic moment in the ground state in LMTO is 0.91, 0.93, and 0.68  $\mu_B$ , respectively.

The calculated exchange parameters are listed in Table 2. The parameters are defined as the effective Heisenberg model,  $E = -\sum_{ij} J_{ij} \hat{m}_i \hat{m}_j$ , where each atomic pair is counted twice, and  $\hat{m}_i$  are unit vectors showing the direction of magnetization for magnetic atom  $i$ . Positive (negative) exchange parameters correspond to FM (AFM) coupling. Antiparallel pairs are highlighted in bold.  $N_j$ : number of neighbors of a given type.  $R_{ij}$  (in Å): distance to the given neighbor. D: dimer pair. Z: nearest neighbor along the c axis. DZ: the nearest neighbor along the c axis of the D neighbor. L1, L2: two inequivalent neighbor types between the nearest ladders. A combination of symbols designates links of a path to the other site.  $J_0 = \sum_j J_{ij} \hat{m}_i \hat{m}_j$  is the total exchange coupling between a given site and the rest of the crystal.  $M$  (in  $\mu_B$ ) is the local moment in LMTO.  $J'_0$  is similar



to  $J_0$  but excludes the contribution from the D neighbor.

The nearest-neighbor intradimer exchange coupling (denoted as D) is dominant and quite strong in both YCrB<sub>4</sub> and YMnB<sub>4</sub>. This intradimer exchange coupling is AFM in YCrB<sub>4</sub> and FM in YMnB<sub>4</sub>, consistent with the magnetic ground states determined above based on total energy calculations. The signs of all significant exchange parameters listed in Table 2 for YCrB<sub>4</sub> agree with their relative alignment in the ground state, indicating the absence of any magnetic frustration. In YMnB<sub>4</sub>, only the weak DZ and L2 couplings are frustrated among those listed in Table 2.

The last line in Table 2 lists the  $|J'_0/J_D|$  ratio, where  $J'_0$  is the total exchange coupling of a given magnetic moment to the rest of the lattice, excluding its D neighbor. This ratio is 1.06 in YCrB<sub>4</sub> and only 0.29 in YMnB<sub>4</sub>. Because the total coupling with other dimers is at most comparable with intradimer coupling, the spins of the dimer partners should be strongly correlated in the interesting temperature range where a magnetic phase transition is possible. For YMnB<sub>4</sub> with FM intradimer coupling and much weaker coupling to the rest of the lattice, it is reasonable to assume that each dimer is maximally correlated, i.e., consider it a composite entity with effective spin 1. Because the frustrated DZ and L2 couplings only amount to 15% of  $J'_0$ , the effect of this frustration on magnetic thermodynamics should be negligible. Examination of the exchange parameters in YMnB<sub>4</sub> also shows that the coupling has a three-dimensional character; neither the interlayer nor interladder coupling is anomalously small.

Because the exchange coupling between dimers in YMnB<sub>4</sub> is three-dimensional without significant frustration, it is expected to order antiferromagnetically at a temperature that may be estimated using the mean-field approximation. The total coupling of a dimer to the rest of the crystal is  $2J'_0$ . Treating the spins classically, we obtain  $T_N \sim (2/3)2J'_0/k_B \approx 120$  K.

Now consider YCrB<sub>4</sub>, where strong AFM intradimer coupling favors the formation of a singlet spin-gap state with no magnetic order<sup>62,63</sup>. The singlet spin-gap state competes with the antiferromagnetically ordered state favored by exchange coupling between the dimers. Proceeding similarly to Ref.<sup>63</sup>, we consider a Heisenberg lattice spin-1/2 Hamiltonian where interaction between dimers will be treated on the mean-field level, while the  $4 \times 4$  Hamiltonian of a given dimer will be diagonalized exactly. In this dimer Hamiltonian, interactions with other dimers are represented by effective fields obtained by replacing the spin operators for other dimers by their expectation values. The solution of this quantum mean-field model predicts a QCP between the singlet spin-gap and the magnetically ordered state at  $|J'_0/J_D| = 1$ . With  $|J'_0/J_D| = 1.06$ , YCrB<sub>4</sub> is thus expected to be close to the QCP.

Experimental measurements show that YCrB<sub>4</sub> has a very small magnetic susceptibility, which was attributed

to a small concentration of magnetic impurities<sup>46</sup>. In dimerized spin-gap systems, the magnetic susceptibility is suppressed at temperatures that are small compared to the singlet-triplet energy gap<sup>64-66</sup>. In the mean-field approximation for the interaction between quantum spin-1/2 dimers, the susceptibility is<sup>64-66</sup>

$$\chi = \frac{k_B C}{k_B T (\frac{3}{4} + \frac{1}{4} \exp(2\beta |J_D|)) + 2J'_F}, \quad (1)$$

where it is assumed that  $J_D < 0$ ,  $C$  is the Curie-Weiss constant, and  $J'_F = \sum_j J_{ij}$  with  $J_D$  excluded.

Using  $J_D = -2.2$  mRy from Table 2, we can estimate the singlet-triplet splitting for the isolated dimer Hamiltonian  $H_D = -2J_D \hat{\sigma}_1 \hat{\sigma}_2$  as  $2|J_D| = 4.4$  mRy. (We assume the DFT calculations correspond to mean-field energies  $E_D = -2J_D \hat{m}_1 \hat{m}_2$ .) This corresponds to a temperature of order 700 K, below which the magnetic susceptibility should be suppressed due to the formation of a spin gap.

Exchange parameters for Mg compounds are also listed in Table 2. Mg has a different valence shell electron count from Y. Two quantum spin-dimer magnets, MgCrB<sub>4</sub> and MgMnB<sub>4</sub>, have relatively weaker  $J_D$ , -1.40 and -1.36 mRy, respectively, compared to that of YCrB<sub>4</sub>. Thus, the spin gaps are expected to cause a suppression for the magnetic susceptibility below a temperature of around 450 K. Nevertheless, due to a relatively weaker  $J'_0$ , MgCrB<sub>4</sub> and MgMnB<sub>4</sub> produce similar  $|J'_0/J_D|$  ratios to that of YCrB<sub>4</sub>, 1.10 and 0.83, respectively, and thus are also expected to be close to the QCP.

As for the conventional antiferromagnet, MgFeB<sub>4</sub>, the frustrated L2 coupling only contributes to 2% of  $J'_0$ . Hence, the effect of frustration is weaker than the one for YMnB<sub>4</sub>. On the other hand, the  $|J'_0/J_D|$  ratio of MgFeB<sub>4</sub> is significantly larger than that of YMnB<sub>4</sub> due to MgFeB<sub>4</sub>'s much weaker intradimer coupling and stronger coupling of a dimer to the rest of the crystal. We further estimate  $T_N \sim 220$  K, again, as in the case of YMnB<sub>4</sub>, considering the dimer to be rigidly coupled.

By alloying the dimerized quantum magnets with different  $T$  elements on the  $T$  sublattice or with different  $M$  elements on the  $M$  sublattice, it may be possible to tune the exchange coupling across the QCP, providing a rare platform and abundant candidates for studying the spin-gap QCP.

**Experimental Synthesis.** The synthesis and basic properties of YCrB<sub>4</sub> and YMnB<sub>4</sub> borides have already been reported. In turn, for YFeB<sub>4</sub> and YCoB<sub>4</sub>, the formation of the phases was mentioned, but neither the procedure to produce single-phase samples nor properties were reported<sup>45,46,49-51</sup>. Our experimental interest in Fe- and Co-containing compounds was two-fold: (i) to achieve future targeted properties modifications by fine-tuning of the Fermi level position via aliovalent substitution, the synthesis of corresponding parent ternary phases need to be developed; (ii) such boron-rich layered structures with boron networks analogous to MgB<sub>2</sub> call for experimental verification of the presence or absence of superconductivity in those compounds. We focused

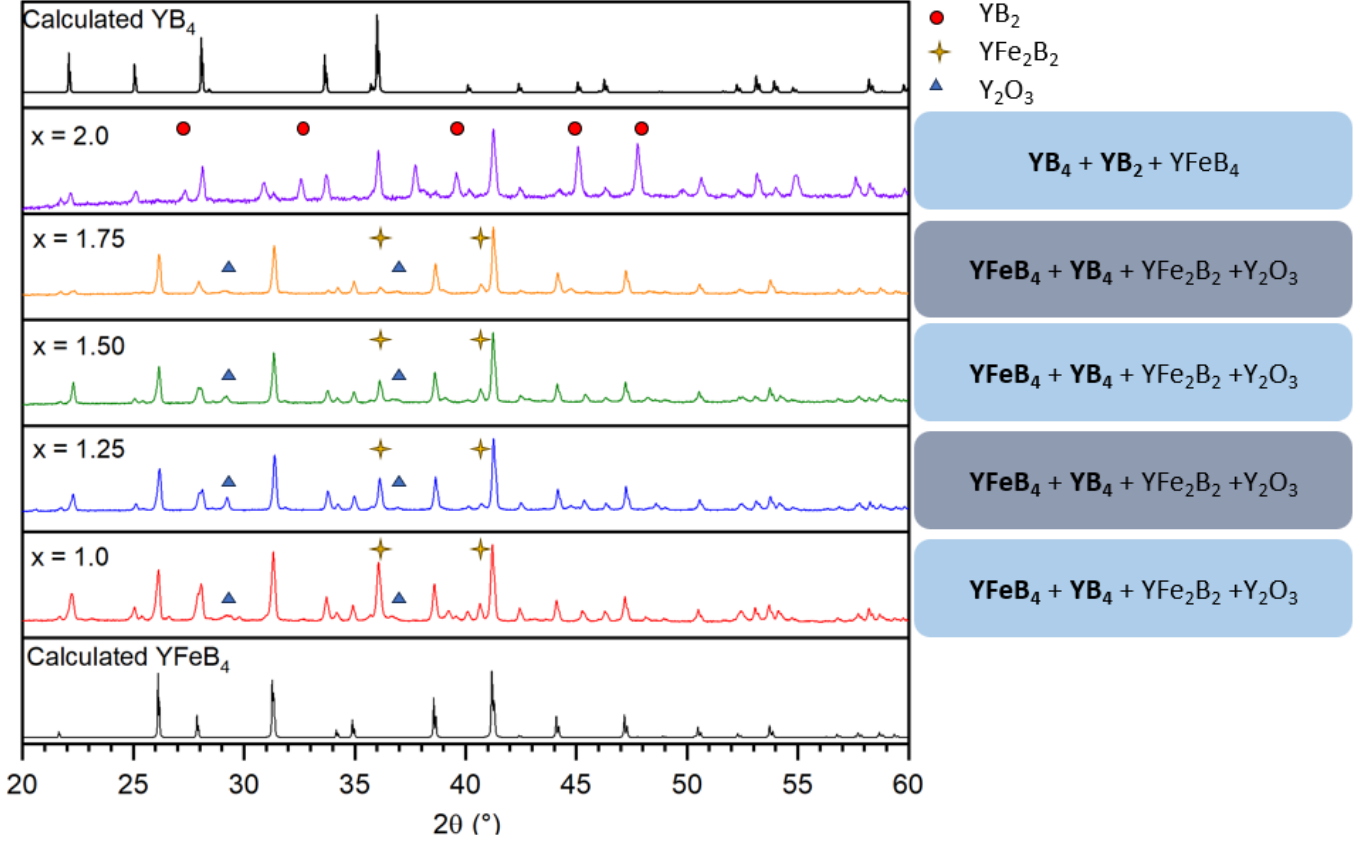


FIG. 6. Experimental powder X-ray diffraction (PXR) patterns (colored) of the arc-melted ingots with varying loaded composition of  $1Y+xFe+4B$ , where  $x = 1.0, 1.25, 1.5, 1.75,$  and  $2.0$ . The values of  $x$  are indicated on the top left corner of the PXR pattern. The calculated patterns of  $YFeB_4$  (based on the single crystal structural model) and  $YB_4$  are shown in black on the bottom and top, respectively. The phase composition for each sample, as determined by PXR, is provided in the boxes to the right. The major phase(s) of each sample are indicated in bold. The most intense peaks of  $Y_2O_3$  (blue triangles),  $YFe_2B_2$  (yellow stars), and  $YB_2$  (red circles) are also indicated.

on the synthesis of  $YFeB_4$  and  $YCoB_4$ . While the formation of  $YCoB_4$  was observed in the experimental samples as one of the major phases, we were not able to reduce the amounts of admixtures to a minimum level, and the properties of  $YCoB_4$  were not investigated.

Arc-melting of the stoichiometric  $YFeB_4$  samples resulted in ingots containing a mixture of two major phases,  $YFeB_4$  and  $YB_4$ , along with minor impurities of  $Y_2O_3$  and  $YFe_2B_2$ . Single crystals of  $YFeB_4$  were obtained, and the crystal structure was refined using single crystal X-ray diffraction (SCXRD). Synthetic efforts were undertaken to characterize  $YFeB_4$  properties, aiming at a single-phase sample of  $YFeB_4$ . To suppress the formation of the  $YB_4$  phase, an excess of Fe was loaded into the starting composition (see Figure 6). As expected, the excess of Fe reduced the formation of  $YB_4$  but resulted in an incomplete elimination of the admixture. Moreover, samples with  $> 25\%$  of Fe excess exhibited an increase in the formation of  $YFe_2B_2$  impurity.

Further treatment was applied to reduce the impurity phases. Heat treatment of the arc-melted ingots for 120 hours at  $1050^\circ C$  was used to improve the homogeneity

of the sample. This allowed for  $YB_4$  and Fe-containing admixture phases to react further and yield  $YFeB_4$  (see Figure 7). Finally, an acid wash in 3M HCl was used to remove some of the remaining impurities, as the target  $YFeB_4$  phase is stable under these acid washing conditions.

Thus, the optimized synthesis of  $YFeB_4$  required the arc-melting of samples containing an Fe excess, 25-50 at.%. After arc-melting, the samples were isothermally annealed at  $1050^\circ C$  for 120 hours, followed by HCl acid washing the finely ground polycrystalline samples overnight (see Figure 7). This optimized synthesis yields  $YFeB_4$  samples with minimal impurities, suitable for basic properties characterization. Characterization of basic properties for  $YFeB_4$  is presented in Text S1 of the Supporting Information.

**Single Crystal Diffraction.** The crystal structure of  $YCrB_4$  was recently redetermined with the single crystal diffraction method<sup>67</sup>. In general, in the structures of borides, mixed occupancy and vacancies in metal sites may occur, which can, in turn, affect the position of the Fermi level and result in properties that are

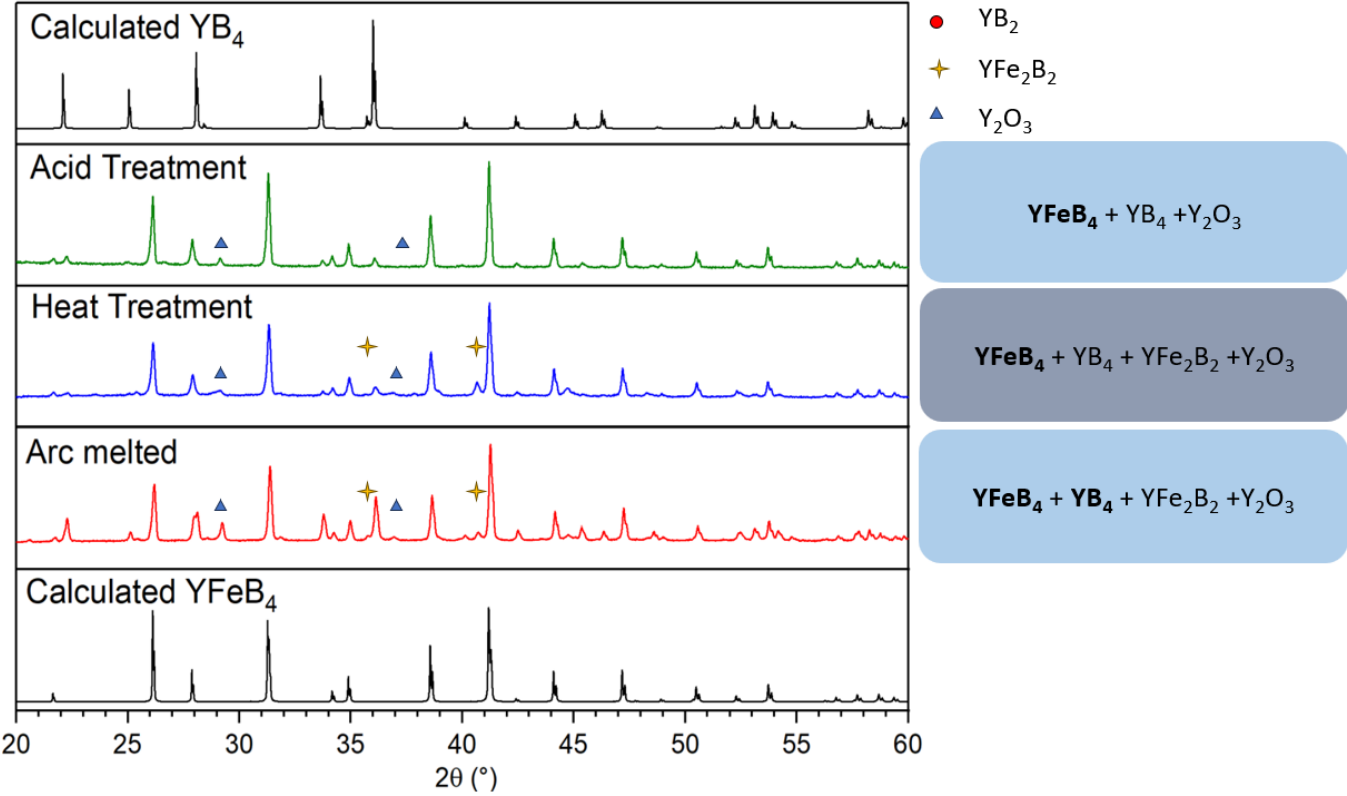


FIG. 7. PXRD patterns of the sample with a loaded composition of  $Y+1.5Fe+4B$ . The sample was arc-melted (red pattern), then annealed isothermally at  $1050\text{ }^{\circ}\text{C}$  for 5 days (blue pattern), followed by being ground into a fine powder and acid washed using 3M HCl (green pattern). Theoretical powder patterns of  $YB_4$  and  $YFeB_4$  (both black) are shown on top and bottom, respectively. The most intense peaks of  $Y_2O_3$  (blue triangles) and  $YFe_2B_2$  (yellow stars) are indicated. The boxes on the right reveal the phase composition of the samples. Bold text indicates a major phase.

different from the expected properties for stoichiometric compounds. We determined the crystal structure of  $YFeB_4$ . The refinement of the single crystal diffraction data reveals 100% occupancy of Fe and Y sites with no Y/Fe mixing or vacancies. In the structure of  $YFeB_4$  determined at 100 K, the B-B distances vary in the 1.689(9)-1.825(7) Å range. This is comparable to the range of B-B distances in  $YCrB_4$  determined at 294 K: 1.72-1.83 Å range. Replacing Cr with Fe resulted in a significant increase in the metal-metal distance in the dimer from 2.374 Å for Cr-Cr to 2.539(1) Å for Fe-Fe. The latter distance agrees with the computationally predicted Fe-Fe distance (2.546 Å,  $\Delta=0.28\%$ ) for the optimized structure. Further details of the crystal structure are provided in Table 3 and in the Supporting Information as a crystallographic information file (CIF).

## CONCLUSIONS

In summary, using first-principles calculations, we identified 21 structurally stable and 25 metastable ternary metal borides of  $MTB_4$ -type ( $M = \text{Sc, Y, La, Ce, Lu, Mg, Ca, Al}$ ;  $T = \text{V, Cr, Mn, Fe, Co, Ni}$ ). Among them, we uncovered 20 magnetic systems, the rest being non-magnetic. Electronic and magnetic

calculations for this family of materials reveal similarities in their electronic and magnetic structures for those compounds with the same valence shell electron count. Magnetism in these compounds is dominated by strong antiferromagnetic Cr (both Cr and Mn for  $M = \text{Mg and Ca}$ ) or ferromagnetic Mn (Fe for  $M = \text{Mg and Ca}$ ) interactions within the structural dimers with much weaker interactions between the dimers. The magnetic ground states in DFT are semiconducting or weakly metallic for these systems. Mn compounds are predicted to be conventional Néel antiferromagnets with layered (A-type) ordering and  $T_N$  below room temperature. In contrast, Cr compounds are proposed to be close to a quantum critical point between a singlet spin-dimer phase, with a spin gap above room temperature, and the conventional Néel antiferromagnetic phase. In total, we unveiled 9 dimerized quantum spin-gap systems and 11 conventional antiferromagnets. 4 of the dimerized quantum magnets are stable ( $\text{ScCrB}_4$ ,  $\text{YCrB}_4$ ,  $\text{LuCrB}_4$ , and  $\text{MgMnB}_4$ ) and 5 are metastable ( $\text{MgCrB}_4$ ,  $\text{CaCrB}_4$ ,  $\text{AlCrB}_4$ ,  $\text{LaCrB}_4$ , and  $\text{CaMnB}_4$ ). They provide a unique possibility for investigating Bose-Einstein condensation of magnetic excitations in crystalline systems<sup>2</sup>. The prediction of this new family of dimerized quantum

TABLE III. Data collection and structure refinement parameters for YFeB<sub>4</sub>. The deposition number 2325813 contains supplementary crystallographic data. These data are provided free of charge by the joint Cambridge Crystallographic Data Centre and FIZ Karlsruhe Access Structures service (<https://www.ccdc.cam.ac.uk/structures>).

Compound	YFeB <sub>4</sub>
CSD-numbers	2325813
temperature (K)	100
radiation (Å)	Mo-K $\alpha$ , 0.71037
crystal system	Orthorhombic
space group	<i>Pbam</i> (no. 55)
<i>a</i> [Å]	5.9049(3)
<i>b</i> [Å]	11.4160(6)
<i>c</i> [Å]	3.4094(2)
Volume [Å <sup>3</sup> ]	229.83(2)
<i>Z</i>	4
data/parameters	533/37
density (g/cm <sup>3</sup> )	5.43
<i>u</i> (mm <sup>-1</sup> )	31.01
<i>R</i> <sub>int</sub>	0.043
GOF	1.38
<i>R</i> <sub>1</sub> [ <i>I</i> > 2 $\sigma$ ( <i>I</i> )]	0.028
<i>wR</i> <sub>2</sub> [ <i>I</i> > 2 $\sigma$ ( <i>I</i> )]	0.078
<i>R</i> <sub>1</sub>	0.030
<i>wR</i> <sub>2</sub>	0.080
diff. peaks [e Å <sup>-3</sup> ]	1.34/-1.31

magnets greatly expands the materials inventory that allows such an investigation<sup>2</sup>. Experimental methods to produce single-phase YFeB<sub>4</sub> suitable for characterization and YFeB<sub>4</sub>'s measured crystal structure are reported. All the stable and metastable *MTB*<sub>4</sub> systems identified in this study, whether quantum-magnetic, conventionally-magnetic, or non-magnetic, provide a platform with numerous possibilities for future doping on the *M* site or the *T* site. Tuning the magnetic exchange coupling by doping may facilitate the study of this rare type of quantum phase transition across the spin-gap quantum critical point. This work offers new opportunities for studying the quantum magnetism of spin dimers in borides. The step-by-step methodology used in this work also demonstrates a theoretical workflow for future searches for dimerized quantum magnets in other families or types of materials.

## METHODS

**Density-Functional Theory Calculations.** We conducted DFT calculations using the projector augmented wave (PAW) method<sup>68</sup> as implemented in the VASP package<sup>69</sup>. The exchange-correlation energy was treated by the Perdew-Burke-Ernzerhof (PBE)<sup>70</sup> generalized gradient approximation (GGA). A plane-wave-basis set was used with a kinetic energy cutoff of 520

eV. The convergence thresholds were 10<sup>-5</sup> eV for electronic self-consistency and 0.01 eV Å<sup>-1</sup> for ionic relaxation. The tetrahedron method with Blöchl corrections was used for the Brillouin zone integration. In the structural optimization, the Brillouin zone was sampled by the Monkhorst-Pack scheme with a k-point grid of  $2\pi \times 0.033 \text{ \AA}^{-1}$ . In the static calculations, energy, magnetic moments, and electronic density of states were computed with a denser k-point grid of  $2\pi \times 0.022 \text{ \AA}^{-1}$ .

**Real-Space Paramagnetic Pauli Spin Susceptibility Matrix Calculations.** Electronic instabilities suggest that analysis of the possibility of local magnetic moments and magnetic order stabilization is required. Take Y compounds, for example. As discussed in the main text, Fe, Co, and Ni compounds are good metals, but according to the Stoner criterion, their  $N(E_f)$  is insufficient to generate FM instability. In contrast, in YMnB<sub>4</sub>, the Fermi level is located at a peak with  $N(E_f) > 1 \text{ eV}^{-1} \text{ f.u.}^{-1} \text{ spin}^{-1}$ . Thus, ferromagnetism in Mn compounds is plausible, while the insulating state of Cr compounds suggests antiferromagnetism as the most likely option. Accordingly, we calculated the real-space paramagnetic Pauli spin susceptibility matrix (see details in Ref.<sup>71</sup>) for transition metal atoms and their neighbors. As expected, the important elements of  $\chi_{ij}$  involve transition-metal atoms and their dimer partners. The on-site term  $\chi_{00}$  dominates, and the intradimer matrix element  $\chi_{ij}$  is about 10% of the former in magnitude. The Anderson local moment criterion ( $S_{00} = I\chi_{00} > 1$ ) is barely satisfied in Mn ( $S_{00} = 1.08$ ), marginal in Cr ( $S_{00} = 0.98$ ), and not satisfied in all other systems. However, the generalization of the Anderson local moment criterion is satisfied for a FM dimer in YMnB<sub>4</sub> with  $I(\chi_{00} + \chi_{01}) = 1.2$  and for an AFM dimer in YCrB<sub>4</sub> with  $I(\chi_{00} - \chi_{01}) = 1.1$ . For all other systems, local moments on a single dimer are unstable. Thus, while the local magnetic instability on Cr and Mn atoms is likely, the resulting atomic moment can be classified as weakly local. This can be compared to strong local moment systems such as bcc iron, where  $S_{00} = 1.6$ <sup>71</sup>. The values obtained above are somewhat similar to the situation in hcp cobalt<sup>71</sup>. However, calculations of susceptibility in cases of weak local moments may not be reliable, and only more precise full-potential self-consistent calculations of the magnetic ground state as seen in the main text can provide a justified answer.

**Synthesis.** High-purity Y fingers (99.9999 %) were acquired from the Materials Preparation Center at Ames National Laboratory. Other chemicals were received from Alfa Aesar: Fe powder (99.9%), Co powder (99.5%), and amorphous B powder (98%). Y fingers were cut into small pieces and weighed out to approximately 230 mg. Based on Y weight and desired molar ratio, i.e., 1:1:4 or 1:1.5:4, Fe and amorphous B amounts were recalculated and weighed out. The mixture of Fe and B was then cold pressed into a pellet. The total sample weight (Y+Fe+B) was approximately 500 mg. Yttrium pieces and the (Fe+4B) pellet were placed onto a water-cooled copper hearth in a tungsten anode arc melter. The cham-

ber was evacuated for 20 minutes and filled with Ar gas. Additionally, a Zr getter was placed in the chamber and arced to remove any traces of oxygen. The  $\text{YFeB}_4$  sample was arc-melted, and then the ingot was flipped and re-melted. This process was repeated four times. A similar procedure was applied for Co-containing samples.

**Annealing.** After arc melting, selected samples were loaded into a carbonized silica ampoule, which was evacuated and flamed sealed. The ampoules were placed into a muffle furnace and heated to  $1050^\circ\text{C}$  with a heating rate of  $175^\circ\text{C}$  per hour. Once at  $1050^\circ\text{C}$ , the samples were isothermally annealed for 120 h. The furnace was turned off and allowed to cool. After annealing, the ingot sample was ground into a fine powder using a tungsten carbide mortar in air.

Selected annealed samples were acid-washed to reduce impurities. Our studies indicated that the target  $\text{YFeB}_4$  phase is acid-stable. The samples were washed in 3M hydrochloric acid overnight to remove  $\text{YB}_4$  and any Fe impurities. After that, the sample was filtered, washed with distilled water, and dried on air.

**Powder X-ray Diffraction (PXRD).** The samples were characterized using powder X-ray diffraction (PXRD) on a Rigaku MiniFlex 600 powder diffractometer with  $\text{Cu-K}_\alpha$  radiation ( $\lambda = 1.54059 \text{ \AA}$ ) and a  $\text{Ni-K}_\beta$  filter. Fluorescence reduction was used to minimize background fluorescence from Fe.

**Single Crystal X-ray Diffraction (SCXRD).** Single crystals of  $\text{YFeB}_4$  were picked out from a crushed ingot with a loaded composition of  $\text{Y+Fe+4B}$ . No further treatment was done to the ingot after arc melting. Single crystal diffraction experiment was conducted using a Bruker D8 Venture diffractometer with a PHOTON detector and  $\text{Mo-K}_\alpha$  radiation. The crystal was cooled to 100 K with a stream of nitrogen gas. Structure determination and the final refinement of the dataset were carried out using the SHELX suite of programs. Refining of the occupancies of Fe and Y indicated no deviations from 100% within one standard uncertainty.

**Scanning Electron Microscopy and Energy Dispersion X-ray Spectroscopy (SEM EDS).** Elemental analysis was carried out using an FEI Quanta 250 field emission SEM with an EDS detector (Oxford X-Max 80, ThermoFischer Scientific, Inc.). The resulting data were analyzed using the Aztec software. Powdered samples were mounted in epoxy, polished to a level surface, and coated with a conductive layer of carbon. An accelerating voltage of 15 kV was used. Compositions were normalized with respect to 1 Y atom to provide information about the Y:Fe ratio. The quantification of light elements, such as B, is not accurate using this technique, but the presence of B was evident from EDS spectra and elemental mapping (see Figure S4 of the Supporting Information).

**Magnetic Measurements.** Magnetic properties were measured by an MPMS-XL SQUID magnetometer (Quantum Design) on two polycrystalline  $\text{YFeB}_4$  samples. The temperature dependence of the magnetic sus-

ceptibility was measured from 2 K to 300 K at applied magnetic fields of 0.1 T and 2T. The isothermal magnetization field dependence was measured from  $-7 \text{ T}$  to  $7 \text{ T}$  at 2 K and 300 K.

**Resistivity Measurements.** A physical property measurement system (PPMS, Quantum Design) was used to characterize the electrical resistivity of the arc-melted ingot of  $\text{YFeB}_4$  (see Figure S5 of the Supporting Information). The ingot was sanded down until a smooth flat surface remained. 50 mm platinum wire was attached to the smooth surface using conductive silver paste. A four-probe method was used for the measurements.

**Heat Capacity Measurements.** Heat capacity was measured from 3.5-300 K using the heat capacity option of the Quantum Design Physical Property Measurement System. The small part of the ingot (13.4 mg) was mounted to the sample platform with Apiezon “N” grease. An addenda measurement containing the heat capacity of the grease was subtracted from the total heat capacity.

## ACKNOWLEDGMENT

This work is supported by the U.S. Department of Energy (DOE) Established Program to Stimulate Competitive Research (EPSCoR) Grant No. DE-SC0024284. Computations were performed at the High Performance Computing facility at Iowa State University and the Holland Computing Center at the University of Nebraska.

## REFERENCES

- (1) Balents, L. Spin Liquids in Frustrated Magnets. *Nature* **2010**, *464*, 199–208. <https://doi.org/10.1038/nature08917>.
- (2) Zapf, V.; Jaime, M.; Batista, C. D. Bose-Einstein condensation in quantum magnets. *Rev. Mod. Phys.* **2014**, *86*, 563–614. <https://doi.org/10.1103/REVMODPHYS.86.563>.
- (3) Matsumoto, M.; Normand, B.; Rice, T. M.; Sigrist, M. Field- and pressure-induced magnetic quantum phase transitions in  $\text{TiCuCl}_3$ . *Phys. Rev. B* **2004**, *69*, 054423. <https://doi.org/10.1103/PhysRevB.69.054423>.
- (4) Sebastian, S. E.; Harrison, N.; Batista, C. D.; Balicas, L.; Jaime, M.; Sharma, P. A.; Kawashima, N.; Fisher, I. R. Dimensional reduction at a quantum critical point. *Nature* **2006**, *441*, 617–620. <https://doi.org/10.1038/nature04732>.
- (5) Nikuni, T.; Oshikawa, M.; Oosawa, A.; Tanaka, H. Bose-Einstein condensation of dilute magnons in  $\text{TiCuCl}_3$ . *Phys. Rev. Lett.* **2000**, *84*, 5868. <https://doi.org/10.1103/PhysRevLett.84.5868>.
- (6) Kodama, K.; Takigawa, M.; Horvatić, M.; Berthier, C.; Kageyama, H.; Ueda, Y.; Miyahara, S.; Becca, F.; Mila, F. Magnetic superstructure in the two-dimensional quantum antiferromagnet  $\text{SrCu}_2(\text{BO}_3)_2$ . *Science* **2002**, *298*, 395–399. <https://doi.org/10.1126/SCIENCE.1075045>.
- (7) Rüegg, C.; Cavadini, N.; Furrer, A.; Güdel, H. U.; Krämer, K.; Mutka, H.; Wildes, A.; Habicht, K.;



- Vorderwisch, P. Bose–Einstein condensation of the triplet states in the magnetic insulator  $\text{TlCuCl}_3$ . *Nature* **2003**, *423*, 62–65. <https://doi.org/10.1038/nature01617>.
- (8) Jaime, M.; Correa, V. F.; Harrison, N.; Batista, C. D.; Kawashima, N.; Kazuma, Y.; Jorge, G. A.; Stern, R.; Heinmaa, I.; Zvyagin, S. A.; Sasago, Y.; Uchinokura, K. Magnetic-field-induced condensation of triplons in Han Purple pigment  $\text{BaCuSi}_2\text{O}_6$ . *Phys. Rev. Lett.* **2004**, *93*, 087203. <https://doi.org/10.1103/PHYSREVLETT.93.087203>.
- (9) Rüegg, C.; McMorrow, D. F.; Normand, B.; Rønnow, H. M.; Sebastian, S. E.; Fisher, I. R.; Batista, C. D.; Gvasaliya, S. N.; Niedermayer, C.; Stahn, J. Multiple magnon modes and consequences for the Bose-Einstein condensed phase in  $\text{BaCuSi}_2\text{O}_6$ . *Phys. Rev. Lett.* **2007**, *98*, 017202. <https://doi.org/10.1103/PHYSREVLETT.98.017202>.
- (10) Sengupta, P.; Batista, C. D. Field-induced super-solid phase in spin-one Heisenberg models. *Phys. Rev. Lett.* **2007**, *98*, 227201. <https://doi.org/10.1103/PHYSREVLETT.98.227201>.
- (11) Stone, M. B.; Lumsden, M. D.; Chang, S.; Samulon, E. C.; Batista, C. D.; Fisher, I. R. Singlet-triplet dispersion reveals additional frustration in the triangular-lattice dimer compound  $\text{Ba}_3\text{Mn}_2\text{O}_8$ . *Phys. Rev. Lett.* **2008**, *100*, 237201. <https://doi.org/10.1103/PHYSREVLETT.100.237201>.
- (12) Samulon, E. C.; Jo, Y. J.; Sengupta, P.; Batista, C. D.; Jaime, M.; Balicas, L.; Fisher, I. R. Ordered magnetic phases of the frustrated spin-dimer compound  $\text{Ba}_3\text{Mn}_2\text{O}_8$ . *Phys. Rev. B* **2008**, *77*, 214441. <https://doi.org/10.1103/PHYSREVB.77.214441>.
- (13) Samulon, E. C.; Kohama, Y.; McDonald, R. D.; Shapiro, M. C.; Al-Hassanieh, K. A.; Batista, C. D.; Jaime, M.; Fisher, I. R. Asymmetric quintuplet condensation in the frustrated  $S=1$  spin dimer compound  $\text{Ba}_3\text{Mn}_2\text{O}_8$ . *Phys. Rev. Lett.* **2009**, *103*, 047202. <https://doi.org/10.1103/PHYSREVLETT.103.047202>.
- (14) Oosawa, A.; Fujisawa, M.; Osakabe, T.; Kakurai, K.; Tanaka, H. Neutron diffraction study of the pressure-induced magnetic ordering in the spin gap system  $\text{TlCuCl}_3$ . *J. Phys. Soc. Jpn.* **2003**, *72*, 1026–1029. <https://doi.org/10.1143/JPSJ.72.1026>.
- (15) Tanaka, H.; Goto, K.; Fujisawa, M.; Ono, T.; Uwatoko, Y. Magnetic ordering under high pressure in the quantum spin system  $\text{TlCuCl}_3$ . *Physica B: Condens. Matter* **2003**, *329–333*, 697–698. [https://doi.org/10.1016/S0921-4526\(02\)02009-4](https://doi.org/10.1016/S0921-4526(02)02009-4).
- (16) Rüegg, C.; Furrer, A.; Sheptyakov, D.; Strässle, T.; Krämer, K. W.; Güdel, H. U.; Mélési, L. Pressure-induced quantum phase transition in the spin-liquid  $\text{TlCuCl}_3$ . *Phys. Rev. Lett.* **2004**, *93*, 257201. <https://doi.org/10.1103/PHYSREVLETT.93.257201>.
- (17) Rüegg, C.; Normand, B.; Matsumoto, M.; Furrer, A.; McMorrow, D. F.; Krämer, K. W.; Güdel, H. U.; Gvasaliya, S. N.; Mutka, H.; Boehm, M. Quantum magnets under pressure: controlling elementary excitations in  $\text{TlCuCl}_3$ . *Phys. Rev. Lett.* **2008**, *100*, 205701. <https://doi.org/10.1103/PHYSREVLETT.100.205701>.
- (18) Merchant, P.; Normand, B.; Krämer, K. W.; Boehm, M.; McMorrow, D. F.; Rüegg, C. Quantum and classical criticality in a dimerized quantum antiferromagnet. *Nat. Phys.* **2014**, *10*, 373–379. <https://doi.org/10.1038/nphys2902>.
- (19) Oosawa, A.; Ono, T.; Tanaka, H. Impurity-induced antiferromagnetic ordering in the spin gap system  $\text{TlCuCl}_3$ . *Phys. Rev. B* **2002**, *66*, 020405. <https://doi.org/10.1103/PhysRevB.66.020405>.
- (20) Manna, S.; Majumder, S.; De, S. K. Tuning of the spin gap transition of spin dimer compound  $\text{Ba}_3\text{Mn}_2\text{O}_8$  by doping with La and V. *J. Phys.: Condens. Matter* **2009**, *21*, 236005. <https://doi.org/10.1088/0953-8984/21/23/236005>.
- (21) Rice, T. M. Quantum mechanics: To condense or not to condense. *Science* **2002**, *298*, 760–761. <https://doi.org/10.1126/SCIENCE.1078819>.
- (22) Sasago, Y.; Uchinokura, K.; Zheludev, A.; Shirane, G. Temperature-dependent spin gap and singlet ground state in  $\text{BaCuSi}_2\text{O}_6$ . *Phys. Rev. B* **1997**, *55*, 8357. <https://doi.org/10.1103/PhysRevB.55.8357>.
- (23) Uchida, M.; Tanaka, H.; Mitamura, H.; Ishikawa, F.; Goto, T. High-field magnetization process in the  $\text{Ba}_3\text{Mn}_2\text{O}_8$ . *Phys. Rev. B* **2002**, *66*, 054429. <https://doi.org/10.1103/PhysRevB.66.054429>.
- (24) Matkovich, V. I., Ed. *Boron and Refractory Borides*; Springer: Berlin, 1977. <https://doi.org/10.1007/978-3-642-66620-9>.
- (25) Scheifers, J. P.; Zhang, Y.; Fokwa, B. P. T. Boron: Enabling exciting metal-rich structures and magnetic properties. *Acc. Chem. Res.* **2017**, *50*, 2317–2325. <https://doi.org/10.1021/ACS.ACCOUNTS.7B00268>.
- (26) Akopov, G.; Yeung, M. T.; Kaner, R. B. Rediscovering the crystal chemistry of borides. *Adv. Mater.* **2017**, *29*, 1604506. <https://doi.org/10.1002/ADMA.201604506>.
- (27) Zhang, S.; Wang, Q.; Kawazoe, Y.; Jena, P. Three-dimensional metallic boron nitride. *J. Am. Chem. Soc.* **2013**, *135*, 18216–18221. <https://doi.org/10.1021/JA410088Y>.
- (28) Mbarki, M.; St. Touzani, R.; Fokwa, B. P. T. Unexpected synergy between magnetic iron chains and stacked  $\text{B}_6$  Rings in  $\text{Nb}_6\text{Fe}_{1-x}\text{Ir}_{6+x}\text{B}_8$ . *Angew. Chem.* **2014**, *126*, 13390–13393. <https://doi.org/10.1002/ANGE.201406397>.
- (29) Shankhari, P.; Bakshi, N. G.; Zhang, Y.; Stekovic, D.; Itkis, M. E.; Fokwa, B. P. T. A delicate balance between antiferromagnetism and ferromagnetism: Theoretical and experimental studies of  $\text{A}_2\text{MRu}_5\text{B}_2$  ( $\text{A}=\text{Zr}, \text{Hf}$ ;  $\text{M}=\text{Fe}, \text{Mn}$ ) metal borides. *Chem. - Eur. J.* **2020**, *26*, 1979–1988. <https://doi.org/10.1002/CHEM.201904572>.
- (30) Sharma, N.; Zhang, Y.; Mbarki, M.; Scheifers, J. P.; Yubuta, K.; Kimber, S. A. J.; Fokwa, B. P. T.  $\text{Nb}_6\text{Mn}_{1-x}\text{Ir}_{6+x}\text{B}_8$  ( $x=0.25$ ): A ferrimagnetic boride containing planar  $\text{B}_6$  rings interacting with ferromagnetic Mn chains. *J. Phys. Chem. C* **2021**, *125*, 13635–13640.

<https://doi.org/10.1021/ACS.JPCC.1C02662>.

(31) Scheifers, J. P.; Flores, J. H.; Janka, O.; Pöttgen, R.; Fokwa, B. P. T. Triangular arrangement of ferromagnetic iron chains in the high- $T_C$  ferromagnet  $\text{TiFe}_{1-x}\text{Os}_{2+x}\text{B}_2$ . *Chem. - Eur. J.* **2022**, *28*, e202201058. <https://doi.org/10.1002/CHEM.202201058>.

(32) Park, H.; Encinas, A.; Scheifers, J. P.; Zhang, Y.; Okwa, B. P. T. F. Boron-dependency of molybdenum boride electrocatalysts for the hydrogen evolution reaction. *Angew. Chem. Int. Ed.* **2017**, *56*, 5575–5578. <https://doi.org/10.1002/ANIE.201611756>.

(33) Jothi, P. R.; Zhang, Y.; Yubuta, K.; Culver, D. B.; Conley, M.; Fokwa, B. P. T. Abundant vanadium diboride with graphene-like boron layers for hydrogen evolution. *ACS Appl. Energy Mater.* **2019**, *2*, 176–181. <https://doi.org/10.1021/ACSAEM.8B01615>.

(34) Woo, K. E.; Kong, S.; Chen, W.; Chang, T. H.; Viswanathan, G.; Díez, A. M.; Sousa, V.; Kolen'ko, Y. V.; Lebedev, O. I.; Costa Figueiredo, M.; Kovnir, K. Topotactic  $\text{BI}_3$ -assisted borodization: synthesis and electrocatalysis applications of transition metal borides. *J. Mater. Chem. A* **2022**, *10*, 21738–21749. <https://doi.org/10.1039/D2TA04266E>.

(35) Saglik, K.; Mete, B.; Terzi, I.; Candolfi, C.; Aydemir, U.; Saglik, K.; Mete, B.; Terzi, I. Thermoelectric borides: Review and future perspectives. *Adv. Phys. Res.* **2023**, 2300010. <https://doi.org/10.1002/APXR.202300010>.

(36) Yeung, M. T.; Mohammadi, R.; Kaner, R. B. Ultraincompressible, superhard materials. *Annu. Rev. Mater. Res.* **2016**, *46*, 465–485. <https://doi.org/10.1146/ANNUREV-MATSCI-070115-032148>.

(37) Akopov, G.; Roh, I.; Sobell, Z. C.; Yeung, M. T.; Pangilinan, L.; Turner, C. L.; Kaner, R. B. Effects of variable boron concentration on the properties of superhard tungsten tetraboride. *J. Am. Chem. Soc.* **2017**, *139*, 17120–17127. <https://doi.org/10.1021/JACS.7B08706>.

(38) Akopov, G.; Yeung, M. T.; Roh, I.; Sobell, Z. C.; Yin, H.; Mak, W. H.; Khan, S. I.; Kaner, R. B. Effects of dodecaboride-forming metals on the properties of superhard tungsten tetraboride. *Chem. Mater.* **2018**, *30*, 3559–3570. <https://doi.org/10.1021/ACS.CHEMMATER.8B01464>.

(39) Akopov, G.; Yeung, M. T.; Sobell, Z. C.; Turner, C. L.; Lin, C. W.; Kaner, R. B. Superhard mixed transition metal dodecaborides. *Chem. Mater.* **2016**, *28*, 6605–6612. <https://doi.org/10.1021/ACS.CHEMMATER.6B02632>.

(40) Nagamatsu, J.; Nakagawa, N.; Muranaka, T.; Zenitani, Y.; Akimitsu, J. Superconductivity at 39 K in magnesium diboride. *Nature* **2001**, *410*, 63–64. <https://doi.org/10.1038/35065039>.

(41) Kortus, J.; Mazin, I. I.; Belashchenko, K. D.; Antropov, V. P.; Boyer, L. L. Superconductivity of metallic boron in  $\text{MgB}_2$ . *Phys. Rev. Lett.* **2001**, *86*, 4656. <https://doi.org/10.1103/PhysRevLett.86.4656>.

(42) An, J. M.; Pickett, W. E. Superconductivity of

$\text{MgB}_2$ : Covalent bonds driven metallic. *Phys. Rev. Lett.* **2001**, *86*, 4366. <https://doi.org/10.1103/PhysRevLett.86.4366>.

(43) Liu, A. Y.; Mazin, I. I.; Kortus, J. Beyond Eliashberg superconductivity in  $\text{MgB}_2$ : Anharmonicity, two-phonon scattering, and multiple gaps. *Phys. Rev. Lett.* **2001**, *87*, 087005. <https://doi.org/10.1103/PhysRevLett.87.087005>.

(44) Gutfleisch, O.; Willard, M. A.; Brück, E.; Chen, C. H.; Sankar, S. G.; Liu, J. P. Magnetic materials and devices for the 21st century: Stronger, lighter, and more energy efficient. *Adv. Mater.* **2011**, *23*, 821–842. <https://doi.org/10.1002/ADMA.201002180>.

(45) Simonson, J. W.; Poon, S. J. Applying an electron counting rule to screen prospective thermoelectric alloys: The thermoelectric properties of  $\text{YCrB}_4$  and  $\text{Er}_3\text{CrB}_7$ -type phases. *J. Alloys. Compd.* **2010**, *504*, 265–272. <https://doi.org/10.1016/J.JALLCOM.2010.05.110>.

(46) Flipo, S.; Rosner, H.; Bobnar, M.; Kvashnina, K. O.; Leithe-Jasper, A.; Gumenuik, R. Thermoelectricity and electronic properties of  $\text{Y}_{1-x}\text{Ce}_x\text{CrB}_4$ . *Phys. Rev. B* **2021**, *103*, 195121. <https://doi.org/10.1103/PHYSREVB.103.195121>.

(47) Candan, A.; Surucu, G.; Gencer, A. Electronic, mechanical and lattice dynamical properties of  $\text{YXB}_4$  ( $X = \text{Cr, Mn, Fe, and Co}$ ) compounds. *Phys. Scr.* **2019**, *94*, 125710. <https://doi.org/10.1088/1402-4896/AB473E>.

(48) Akopov, G.; Pangilinan, L. E.; Mohammadi, R.; Kaner, R. B. Perspective: Superhard metal borides: A look forward. *APL Mater.* **2018**, *6*, 70901. <https://doi.org/10.1063/1.5040763>.

(49) Akopov, G.; Yin, H.; Roh, I.; Pangilinan, L. E.; Kaner, R. B. Investigation of hardness of ternary borides of the  $\text{YCrB}_4$ ,  $\text{Y}_2\text{ReB}_6$ ,  $\text{Y}_3\text{ReB}_7$ , and  $\text{YMo}_3\text{B}_7$  structural types. *Chem. Mater.* **2018**, *30*, 6494–6502. <https://doi.org/10.1021/ACS.CHEMMATER.8B03008>.

(50) Kuzma, Y. B. Crystal structure of the  $\text{YCrB}_4$  compound and its analogs. *Sov. Phys. Crystallogr.* **1970**, *15*, 372–374.

(51) Kuzma, Y. B. New ternary compounds with the structure of  $\text{YCrB}_4$  type. *Dopov. Akad. Nauk Ukr. RSR Ser. A* **1970**, *8*, 756–758.

(52) Rogl, P. Chapter 6.7.2.3 Borides with two-dimensional boron networks. *Inorganic Reactions and Methods* **1991**, *13*, 156–167. <https://doi.org/10.1002/9780470145289.CH26>.

(53) Rogl, P. Chapter 49 Phase equilibria in ternary and higher order systems with rare earth elements and boron. *Handbook on the Physics and Chemistry of Rare Earths* **1984**, *6*, 335–523. [https://doi.org/10.1016/S0168-1273\(84\)06006-2](https://doi.org/10.1016/S0168-1273(84)06006-2).

(54) Rogl, P. New ternary borides with  $\text{YCrB}_4$ -type structure. *Mater. Res. Bull.* **1978**, *13*, 519–523. [https://doi.org/10.1016/0025-5408\(78\)90160-5](https://doi.org/10.1016/0025-5408(78)90160-5).

(55) Medvedeva, N. I.; Medvedeva, Y. E.; Ivanovskii, A. L. Electronic structure of ternary boron-containing phases  $\text{YCrB}_4$ ,  $\text{Y}_2\text{ReB}_6$ , and  $\text{MgC}_2\text{B}_2$ . *Dokl. Phys.*

- Chem.* **2002**, *383*, 75–77. <https://doi.org/10.1023/A:1014734530591>.
- (56) Sun, Y.; Zhang, Z.; Porter, A. P.; Kovnir, K.; Ho, K. M.; Antropov, V. Prediction of Van Hove singularity systems in ternary borides. *npj Comput. Mater.* **2023**, *9*, 1–11. <https://doi.org/10.1038/s41524-023-01156-8>.
- (57) Jain, A.; Ong, S. P.; Hautier, G.; Chen, W.; Richards, W. D.; Dacek, S.; Cholia, S.; Gunter, D.; Skinner, D.; Ceder, G.; Persson, K. A. Commentary: The materials project: A materials genome approach to accelerating materials innovation. *APL Mater.* **2013**, *1*, 011002. <https://doi.org/10.1063/1.4812323>.
- (58) Kirklin, S.; Saal, J. E.; Meredig, B.; Thompson, A.; Doak, J. W.; Aykol, M.; Rühl, S.; Wolverton, C. The Open Quantum Materials Database (OQMD): assessing the accuracy of DFT formation energies. *npj Comput. Mater.* **2015**, *1*, 1–15. <https://doi.org/10.1038/npjcompumats.2015.10>.
- (59) Sun, W.; Dacek, S. T.; Ong, S. P.; Hautier, G.; Jain, A.; Richards, W. D.; Gamst, A. C.; Persson, K. A.; Ceder, G. The thermodynamic scale of inorganic crystalline metastability. *Sci. Adv.* **2016**, *2*, e1600225. <https://doi.org/10.1126/SCIADV.1600225>.
- (60) Liechtenstein, A. I.; Katsnelson, M. I.; Antropov, V. P.; Gubanov, V. A. Local spin density functional approach to the theory of exchange interactions in ferromagnetic metals and alloys. *J. Magn. Magn. Mater.* **1987**, *67*, 65–74. [https://doi.org/10.1016/0304-8853\(87\)90721-9](https://doi.org/10.1016/0304-8853(87)90721-9).
- (61) Pashov, D.; Acharya, S.; Lambrecht, W. R. L.; Jackson, J.; Belashchenko, K. D.; Chantis, A.; Jamet, F.; van Schilfgaarde, M. Questaal: A package of electronic structure methods based on the linear muffin-tin orbital technique. *Comput. Phys. Commun.* **2020**, *249*, 107065. <https://doi.org/10.1016/J.CPC.2019.107065>.
- (62) Kato, T.; Oosawa, A.; Takatsu, K.; Tanaka, H.; Shiramura, W.; Nakajima, K.; Kakurai, K. Magnetic excitations in the spin gap system  $\text{KCuCl}_3$  and  $\text{TlCuCl}_3$ . *J. Phys. Chem. Solids* **1999**, *60*, 1125–1128. [https://doi.org/10.1016/S0022-3697\(99\)00072-4](https://doi.org/10.1016/S0022-3697(99)00072-4).
- (63) Zhu, M.; Matsumoto, M.; Stone, M. B.; Dun, Z. L.; Zhou, H. D.; Hong, T.; Zou, T.; Mahanti, S. D.; Ke, X. Amplitude modes in three-dimensional spin dimers away from quantum critical point. *Phys. Rev. Res.* **2019**, *1*, 033111. <https://doi.org/10.1103/PHYSRESEARCH.1.033111>.
- (64) Tanaka, H.; Takatsu, K. I.; Shiramura, W.; Ono, T. Singlet ground state and excitation gap in the double spin chain system  $\text{KCuCl}_3$ . *J. Phys. Soc. Jpn.* **1996**, *65*, 1945–1948. <https://doi.org/10.1143/JPSJ.65.1945>.
- (65) Vinnik, O.; Tarasenko, R.; Orendáč, M.; Orendáčová, A. Dimerized nature of magnetic interactions in the  $S = 1/2$  quantum antiferromagnet  $\text{Cu}(\text{en})_2\text{SO}_4$ . *J. Magn. Magn. Mater.* **2022**, *547*, 168789. <https://doi.org/10.1016/J.JMMM.2021.168789>.
- (66) Carlin, R. L.; van Duynveldt, A. J. Dimers and clusters. In *Magnetic Properties of Transition Metal Compounds*; Springer, Berlin, Heidelberg, 1977; pp 77–108. [https://doi.org/10.1007/978-3-642-87392-8\\_4](https://doi.org/10.1007/978-3-642-87392-8_4).
- (67) Tokuda, M.; Yubuta, K.; Shishido, T.; Sugiyama, K. Redetermination of the crystal structure of yttrium chromium tetraboride,  $\text{YCrB}_4$ , from single-crystal X-ray diffraction data. *Acta Crystallogr. E: Crystallogr. Commun.* **2023**, *79*, 1072–1075. <https://doi.org/10.1107/S2056989023008952>.
- (68) Blöchl, P. E. Projector augmented-wave method. *Phys. Rev. B* **1994**, *50*, 17953. <https://doi.org/10.1103/PhysRevB.50.17953>.
- (69) Kresse, G.; Furthmüller, J. Efficient iterative schemes for *ab initio* total-energy calculations using a plane-wave basis set. *Phys. Rev. B* **1996**, *54*, 11169. <https://doi.org/10.1103/PhysRevB.54.11169>.
- (70) Perdew, J. P.; Burke, K.; Ernzerhof, M. Generalized gradient approximation made simple. *Phys. Rev. Lett.* **1996**, *77*, 3865. <https://doi.org/10.1103/PhysRevLett.77.3865>.
- (71) Samolyuk, G. D.; Antropov, V. P. Character of magnetic instabilities in  $\text{CaFe}_2\text{As}_2$ . *Phys. Rev. B* **2009**, *79*, 052505. <https://doi.org/10.1103/PhysRevB.79.052505>.